Finanziato dall'Unione europea NextGenerationEU | Ministero dell'Università e della Ricerca | Italiadomani PIANO NAZIONALE DI RIPRESA E RESILIENZA

multi-Risk sciEnce for resilienT commUnities undeR a changiNg climate

Codice progetto MUR: **PE00000005** – CUP LEAD PARTNER: I33C22006910006

Deliverable title: Natural Hazards classification maps of point-like infrastructures of national relevance – Validation of Methodologies and Application Report

Deliverable ID: 6.3.2

Due date: September 2025

Submission date: September 2025

AUTHORS

Pierluigi Claps, Daniele Ganora, Paola Mazzoglio, Giulia Evangelista (POLITO), Salvatore Manfreda, Angelo Avino (UNINA); Monica Papini, Laura Longoni, Matteo Antelmi, Monica Corti (POLIMI); Antonello Barresi, David Castro Rodriguez (POLITO), Michele Torregrossa, Maria Castiglione (UNIPA); Paolo De Girolamo, Carolina Codato, Gioele Ruffini (UNIROMA1).

Approved by Paola Mazzoglio (WP leader)

1. Technical references

Project Acronym	RETURN
Project Title	multi-Risk sciEnce for resilienT commUnities undeR a changiNg climate
Project Coordinator	Domenico Calcaterra UNIVERSITA DEGLI STUDI DI NAPOLI FEDERICO II domcalca@unina.it
Project Duration	December 2022 – November 2025 (36 months)

Deliverable No.	DV3.2
Dissemination level*	PU
Work Package	WP3 - Dynamic mapping of natural and climatic hazards over the infrastructure systems
Task	T3.2 - Robust hazard mapping over point critical infrastructures (link with Spokes 1÷3)
Lead beneficiary	POLITO and POLIMI
Contributing beneficiary/ies	POLITO, UNINA, POLIMI, UNIPA, UNIROMA1

* PU = Public

PP = Restricted to other programme participants (including the Commission Services)

RE = Restricted to a group specified by the consortium (including the Commission Services)

CO = Confidential, only for members of the consortium (including the Commission Services)

Document history

Version	Date	Lead contributor	Description
0.1	01.09.2025	POLIMI and POLITO	First draft
0.2	19.09.2025		Critical review and proofreading
0.3	25.09.2025		Edits for approval
1.0	29.09.2025		Final version

2. Abstract

Similarly to Task 3.1, dynamic hazard selection criteria and maps are targeted, with robust and reliable methodologies, to produce hazard classification of individual, point-like critical infrastructures, such as dams, drinking water facilities and wastewater treatment plants. More specifically, the evaluation and mapping of natural hazard risks, particularly floods, sediments erosion, tsunamis and industrial asset vulnerabilities, across different sectors and geographical areas in Italy is taken in account. The main differences with respect to the approaches used in Task 3.1 attain the need to highlight the specific functions of each individual infrastructure, as well as the effects of hazards on the areas and users served.

This deliverable describes the products that were developed within the Task 3.2 of the Spoke TS2 to address these goals, which can be summarized in:

- the creation of a national-scale inventory of the Italian Large Dams complemented with more than 100 different catchment descriptors (Section 3.2.a);
- a national-scale assessment of the intrinsic flood attenuation potential of Italian Large Dams developed to identify the reservoirs best fitted for their flood mitigation efficiency (Section 3.2.a);
- assessment of the impact of dams on flood frequency curves (Section 3.2.a);
- development and application of sediment transport model (catchment-scale) to dam filling prediction and bottom openings interference in different geological contexts influencing sediment erosion and shallow water flow (Section 3.2.a);
- a place-based methodology for territorial vulnerability awareness including high-risk installations (e.g., drinking water and wastewater treatment plants), at various territorial scales (Section 3.2.b);
- development of a methodology aimed at calculating the areas and flooding speeds caused by tsunamis generated by earthquakes (Section 3.3.c).

In summary, all the activities aim to provide a comprehensive understanding of natural multi-hazards in key infrastructure sectors, enabling more informed risk management and mitigation strategies. The methodologies developed in the task are described in the first part of the deliverable (*DV 6.3.2 - Natural Hazards classification maps of point-like infrastructures of national relevance - Methodology Report*). This second part is instead focused on the implementation process and the key results obtained.

3. Table of contents

1. Technical references 3
Document history 4
2. Abstract 5
3. Table of contents 6
List of Figures 8
3.2 Natural Hazards classification maps of point-like infrastructures of national relevance 10
3.2.a Enhanced hydrological hazard assessment on Large Dams 10
3.2.a.1 Flood Attenuation Potential of Italian Large Dams 10
3.2.a.2 Flood Peak Attenuation of Large Dams and Detention basins 11
3.2.a.3 Sediment transport model for dam filling prediction 15
3.2.a.3.1 SMART-SED application to the Camastra catchment 15
3.2.a.3.2 Results and discussion 20
3.2.a.3.3 Results after including landslides phenomena (collaboration with SPOKE VS2) 23
3.2.a.3.4 Conclusions 26
3.2.b Place-based methodology for territorial vulnerability awareness (Using Geographical Information Systems - GIS) 27
3.2.b.1 Vulnerability of areas of concern around industrial assets (Seveso Industries) using a multi-hazard and multi-scale approach 27
3.2.b.1.1 Dataset of industrial assets: Using National Inventory of Major Accident Hazard Establishments. 27
3.2.b.1.2 Classification of industrial assets according to the principal macro-sectors within the process industry and represented regionally 27
3.2.b.1.3 Geo-localization of Industrial assets as Point-like Infrastructures at large scale (national, regional, provincial) and territorial vulnerability representation. 28
3.2.b.1.4 Contextualization of natural and territorial hazards at the scale of interest (lightning phenomena considered as a pilot study). 33
3.2.b.2 Vulnerability assessment of drinking water and wastewater treatment plants as point critical infrastructures using a multi-hazard, multi-scale approach 34
3.2.b.2.1 Dataset of WWTPs: Using data from Istat, Regione Sicilia and managers of integrated water service (Sicilia) 34
3.2.b.2.2 Dataset of DWTPs: Using data from managers of integrated water service (Sicilia) 37
3.2.b.2.3 WWTPs and DWTPs mapping using a multi-hazard multi-scale approach 38
3.2.b.3 Conclusions 39
3.2.c Coastal flooding caused by tsunami waves generated by earthquakes 41
3.2.c.1 Introduction 41
3.2.c.2 Input data and numerical setup 41
3.2.c.2.1 Boundary conditions and numerical grids for step II and step III 41
3.2.c.3 Application of step I 42
3.2.c.4 Application of step II 43
3.2.c.5 Application of step III 44
5. References 46

List of Figures

Figure 1: ECDF curves built for each of the four combinations. Brownish and bluish colours refer to the PMcD's tc and 1.5 PMcD's tc, respectively, while darker or lighter colours refer to a runoff coefficient equal to 1 or 0.5, respectively. The horizontal positions of results in the two highlighted dams (Occhito Dam: Basin area=1014.18 km^2, mean elevation=582 m a.s.l.; Sabbione Dam: basin area=14.28 km^2, mean elevation=2767 m a.s.l.) show that the runoff coefficient has no influence on the ranking stability. 10
Figure 2: Range of variability of the IDF parameters over Italy (grey shaded area), with average values (yellow square). Colour of points stands for the sign of (blue for negative values, red for positive values), while the size refers to the entity of Panel (a) refers to the rectangular hydrograph, panel (b) to the NERC one. 11
Figure 3: Sketch of a detention basin section with a basin capacity W_{max}, composed of a crest spillway of height h_s. 12
Figure 4: Theoretically derived distribution (TDD) of the water level associated with three values of the mean daily rainfall (red I = 1 mm/day, green I = 2 mm/day, blue I = 4 mm/day) using two different values of the time rate of the Poisson process: 0.1 for the left panel and 0.2 for the right one. All the other parameters are: h_s = 5 m; α = 5000 m^3, β = 1.78, A_b = 10 km^2, φ = 0.5. In addition, the daily withdrawals (L) are assumed to be 30% of the incoming discharge. 13
Figure 5: Theoretically derived distribution (TDD) of the water level associated with two values of the coefficient of the stage-storage capacity curve of the dam (α = 3000 and 5000 m^3) using three different values of the height of the spillway crest: 3 m for the left panel, 5 m for the central panel and 8 m for the right one. All the other parameters are: β = 1.78, Ab = 10 km^2, φ = 0.5, Poisson time rate = 0.2, and I = 2 mm/day. In addition, the daily withdrawals (L) are assumed to be 30% of the incoming discharge. . 13
Figure 6: Comparison between the theoretically derived distribution (TDD) of the water level (continuous blue line) and the empirical probability density function (pdf) obtained via numerical hydraulic simulation (dashed red line) for two different values of the height of the spillway crest: 5 m for the left panel and 8 m for the right one. 14
Figure 7: Comparison between the theoretically derived distribution (TDD) of the water level (continuous blue line) and the empirical probability density function (pdf) obtained via numerical hydraulic simulation (dashed red line) for the Camastra dam. 15
Figure 8: Overview of the Camastra catchment and zoom on the Camastra lake. 16
Figure 9: Lithologies present in the Camastra catchment. 17
Figure 10: Spatial distribution of pluviometric stations located neare the Camastra catchment. 18
Figure 11: CORINE Land Cover (2018) map of the study area. 20
Figure 12: Location of the ten simulated control points, with a focus on the Camastra Lake. 21
Figure 13: Discharge at control points no.1, 6 and 8, and rainfall at the Camastra dam during 2021..... 21
Figure 14: Water depth in the Camastra catchment after a rainfall event in November 2021. 22
Figure 15: (a) Total sediment volume estimated as the sum of the contributions of control points 1, 6 and 8 during 2021, compared to the reference value; b) yearly cumulative erosion thickness across the catchment area at the end of 2021..... 22
Figure 16: Annual cumulative erosion in the catchment for the years with minimum, average, and maximum rainfall among the simulated periods. 23
Figure 17: Landslides distribution in the Camastra catchment according to the Italian Landslide Inventory (IFFI)..... 24
Figure 18: Landslide masks used in the simulations: (a) landslide polygons, and (b) landslide-susceptibile areas. 24
Figure 19: Annual cumulative erosion across the Camastra catchment for the year 2012: (a) base simulation without landslide mask, (b) simulation including the landslide polygon mask, and (c) simulation including the landslide susceptibility mask. In cases (b) and (c), erosion was allowed only within the corresponding masks..... 25
Figure 20: Annual cumulative erosion across the Camastra catchment for the year 2012: (a) base simulation without landslide mask, (b) simulation including the landslide polygon mask, and (c) simulation including the landslide susceptibility mask. In cases (b) and (c), erosion was set to high values within the masks, while outside it depended on land cover and lithology, as in the base simulation..... 26
Figure 21: Regional distribution of the industrial macro-sectors for Italian MHIs. 28

Figure 22: Association of MHIs with geophysical information of interest information. a) Map of the locations of the Seveso industrial plants in Italy. Source: Carpanese et al. (2024). b) Italian seismic classification. Source: Dipartimento della Protezione Civile (2023). 29
Figure 23: Representation of Seveso establishment and binding areas in Piedmont and Zoom for sector containing the establishments in the Metropolitan City of Turin. 31
Figure 24: Pareto diagrams: a) Number of Seveso establishments by kind of industrial activities in the Piedmont region. b) Number of Seveso establishments by province in the Piedmont. 32
Figure 25: Density of inhabitants (person·ha^{-1}) in the areas of observation and exclusion by province. 32
Figure 26: Pareto diagram for macro-sectors vulnerability against lightning strikes within the process industry. 33
Figure 27: Multi-scale analysis of wastewater treatment plants. 36
Figure 28: Results from the multi-hazard approach depicting vulnerability between WWTPs and Territory. 38
Figure 29: Results from the multi-hazard approach depicting vulnerability between DWTPs and Territory. 39
Figure 30: Bathymetry and topography of the area used for the inundation simulations. 41
Figure 31: Numerical domains schematisation and detailed application of step II. 42
Figure 32: Definition of the Points of Interest (POIs) and computation of MIHd: (a) map showing the selected POIs, and (b) hazard probability curves at the 84th percentile for each POI. The red circle highlights the intersection between Pevr and the hazard curve of POI 4. 43
Figure 33: Example time series of the N-wave with T = 240 s: (a) offshore signal at t1 and propagated wave at POI 4; (b) input boundary condition for inundation at t2. 44
Figure 34: Aggregated hazard maps of the inundation depth hi for (a) Messina, (b) Villa San Giovanni, and (c) Reggio Calabria with inundation extents of simplified inundation maps from ISPRA. 45

3.2 Natural Hazards classification maps of point-like infrastructures of national relevance

3.2.a Enhanced hydrological hazard assessment on Large Dams

3.2.a.1 Flood Attenuation Potential of Italian Large Dams

The analysis is built upon a simplified yet physically consistent hydrological–hydraulic model. The attenuation coefficient η, the ratio between the peak outflow and the peak inflow discharge, is used as an indicator of flood-attenuation performance (η = 1 means no attenuation; lower values indicate stronger attenuation).

To generate inflow hydrographs, the study employs the rational method to estimate design peak discharges. Two hydrograph shapes are tested, i.e. (i) a simple rectangular hydrograph and (ii) a NERC synthetic hydrograph.

The authors vary three key input parameters to explore sensitivity of flood attenuation potential:

- runoff coefficient (C): 0.5 and 1.0;
- time of concentration (tc): computed by different empirical formulas (Pilgrim–McDermott, Giandotti) and scaled by ±50%;
- IDF parameters (a, n): either uniform averages for all Italy (AVG) or locally derived values for each basin (LOC).

Combinations of these parameters and hydrograph shapes result in 24 simulation scenarios for every dam, providing a basis for both quantitative and ranking analyses of attenuation efficiency.

Main results can be summarized as follows:

i. Influence of runoff coefficient (C): lower C values yield smaller inflow volumes and thus higher attenuation (lower η). However, variations in C have little effect on the relative ranking of dams: while absolute attenuation efficiency changes, their performance order remains largely stable (see Figure 1). This indicates that C primarily acts as a linear scaling factor rather than a driver of ranking variability.

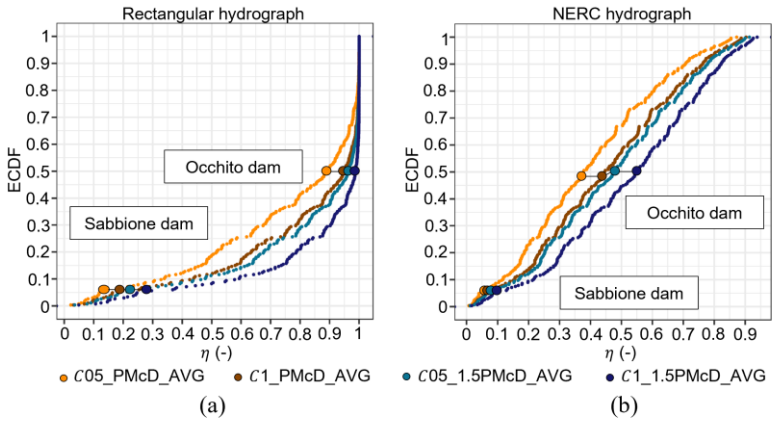

Figure 1: ECDF curves built for each of the four combinations. Brownish and bluish colours refer to the PMcD's tc and 1.5 PMcD's tc, respectively, while darker or lighter colours refer to a runoff coefficient equal to 1 or 0.5, respectively. The horizontal positions of results in the two highlighted dams (Occhito Dam: Basin area=1014.18 km^2, mean elevation=582 m a.s.l.; Sabbione Dam: basin area=14.28 km^2, mean elevation=2767 m a.s.l.) show that the runoff coefficient has no influence on the ranking stability.

ii. Influence of time of concentration (tc): the results show that tc exerts the strongest control among all tested parameters. Food attenuation is highly sensitive to tc, since shorter tc values correspond to shorter duration of the inflow hydrographs, allowing the reservoir to temporarily store a larger portion of the flood volume before the spillway capacity is reached. Linear changes (±50%) in tc, such as switching from PMcD to 1.5PMcD, cause only minor variations in ranking: the maximum displacement is about 3 positions for the rectangular hydrograph and 6 positions for the NERC hydrograph. This indicates a relatively stable classification when tc is scaled uniformly. Changing the formula for tc (e.g., PMcD → Giandotti), which introduces morphological dependencies (slope, stream length), produces much larger effects. Relative ranking changes (ΔR/R) can reach ±200%, meaning that a dam's position in the national attenuation ranking can shift in a substantial way depending on how tc is estimated. This is particularly true for small alpine basins where steep slopes yield much smaller tc when estimated using the PMcD formula.

iii. Influence of climate variability:
incorporating catchment-averaged rainfall intensity–duration–frequency (IDF) parameters (a, n) results in only minor changes in dam rankings. While local climate can significantly influence the value of the attenuation coefficient, causing up to ±50% variation in η values for NERC hyetograph shapes (Figure 2), the overall ranking of efficiency remains largely consistent: 80% of dams shift by fewer than 8–20 positions. This indicates that geomorphic characteristics, rather than climatic variability, are the primary drivers of attenuation performance.

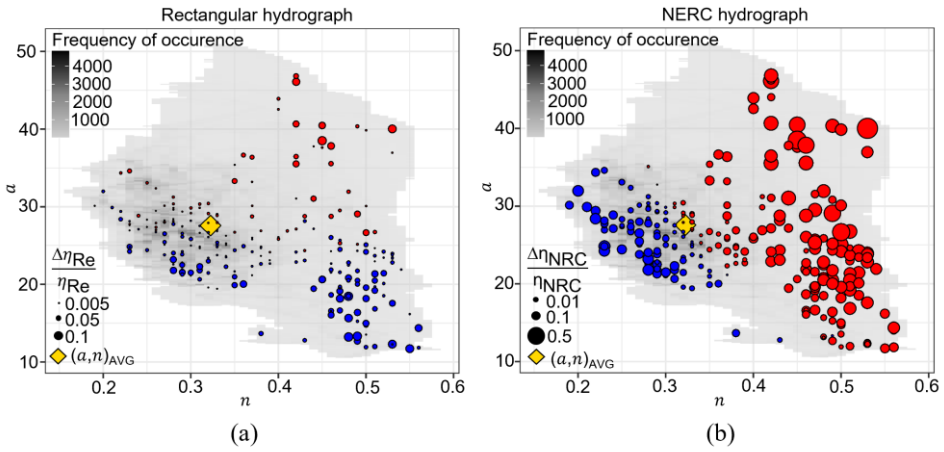

Figure 2: Range of variability of the IDF parameters over Italy (grey shaded area), with average values (yellow square). Colour of points stands for the sign of (blue for negative values, red for positive values), while the size refers to the entity of Panel (a) refers to the rectangular hydrograph, panel (b) to the NERC one.

iv. Influence of hydrograph shape:
The assumed inflow hydrograph shape (rectangular vs NERC) affects the magnitude of η but not the rank ordering. Hence, for large-scale screening or comparative assessments, detailed hydrograph modeling is not essential; however, realistic shapes remain important when evaluating individual dams quantitatively.

These findings mean that broad-scale flood-management planning in Italy can rely on morphological indicators to identify reservoirs offering the highest natural attenuation benefits, without needing highly detailed local hydrological simulations. Moreover, the approach helps prioritize dams for potential integration into coordinated flood-mitigation strategies and informs national flood-frequency analyses by quantifying how much reservoir regulation modifies downstream flood hazards.

3.2.a.2 Flood Peak Attenuation of Large Dams and Detention basins

Dams are commonly implemented to attenuate peak discharges and reduce downstream flood risk, although their impact on flood dynamics is complex, context-dependent, and influenced by hydrologic and hydraulic factors. With this aim, this study explores the impacts of dam systems on flood processes through a new analytical-probabilistic approach.

Over the years, several approaches have been developed to interpret the relationships between inflows and expected outflows from dams. Among the others, (Manfreda et al., 2021) derived a theoretical distribution of peak outflows from detention basins. However, that formulation tends to neglect the reservoir pre-filling from previous flood events, leading to an underestimation of storage volume. With this aim, a new analytical-probabilistic approach to theoretically derive the distribution of the water level in the reservoir has been developed and coupled with the formulation by (Manfreda et al., 2021). The new mathematical framework extends the range of applications of the original formulation by incorporating the initial state of water storage prior to each flood and represents an effective tool for assessing the impacts of dams on flood dynamics.

The new analytical-probabilistic framework has been defined as a joint probability distribution of two theoretically derived distributions (TDD) of i) the peak outflow from the dam and ii) the water level in the reservoir. The TDD of the peak outflow is reported in (Manfreda et al., 2021), while the distribution of water level has been obtained by combining the stage-storage capacity curve of the dam and the probability density function of water volume in the reservoir. The pdf of water volume in the reservoir has been evaluated through the water balance equation by exploiting the approach by (Manfreda & Fiorentino, 2008). Specifically, by considering the mass conservation equation of the water volume in the reservoir, the rainfall forcing is considered as an additive noise (modelled by a sequence of instantaneous pulses that occur in a Poisson process of time rate λ), while the water losses (evaporation and water withdrawal) are assumed to be constant over time.

The expression of the theoretically derived distribution of the water level is:

$$p_H(H) = \beta \frac{\alpha}{W_{max}} H^{\beta-1} \cdot \frac{C}{B*} e^{\left(-\gamma+\frac{\lambda}{B*}\right)\cdot\left(\frac{\alpha}{W_{max}}H^{\beta}\right)} \qquad (3.2.1)$$

where α and β are the parameters of the stage-storage capacity curve of the dam, W_{max} is the maximum storage capacity of the reservoir, B* $\left(B* = \frac{B}{W_{max}}\right)$ represents the dimensionless water losses (evaporation and water withdrawal) and it is assumed to be constant, λ is the rate in time of a Poisson process, γ represents the parameter of the normalized probability density function of the incoming runoff $\gamma = \frac{W_{max}}{\varphi A_b I}$ (where φ [-] is the coefficient of infiltration, A_b $[m^2]$ is the area of the river basin and I [mm/day] is the mean daily rainfall) and C is the constant of integration.

A simplified sketch of detention dam has been considered (see Figure 3), with a basin capacity, W_{max}, and a crest spillway of height h_s.

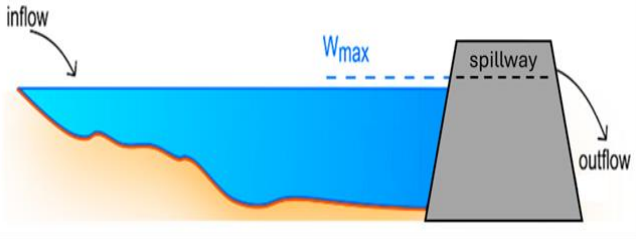

Figure 3: Sketch of a detention basin section with a basin capacity W_{max}, composed of a crest spillway of height h_s.

A sensitivity analysis was performed to assess the influence of the parameters on the patterns of the water level probability distribution. In Figure 4, the TDD is reported for three values of the mean daily rainfall (I = 1, 2, 4 mm/day) using two different values of the time rate of the Poisson process: 0.1 and 0.2.

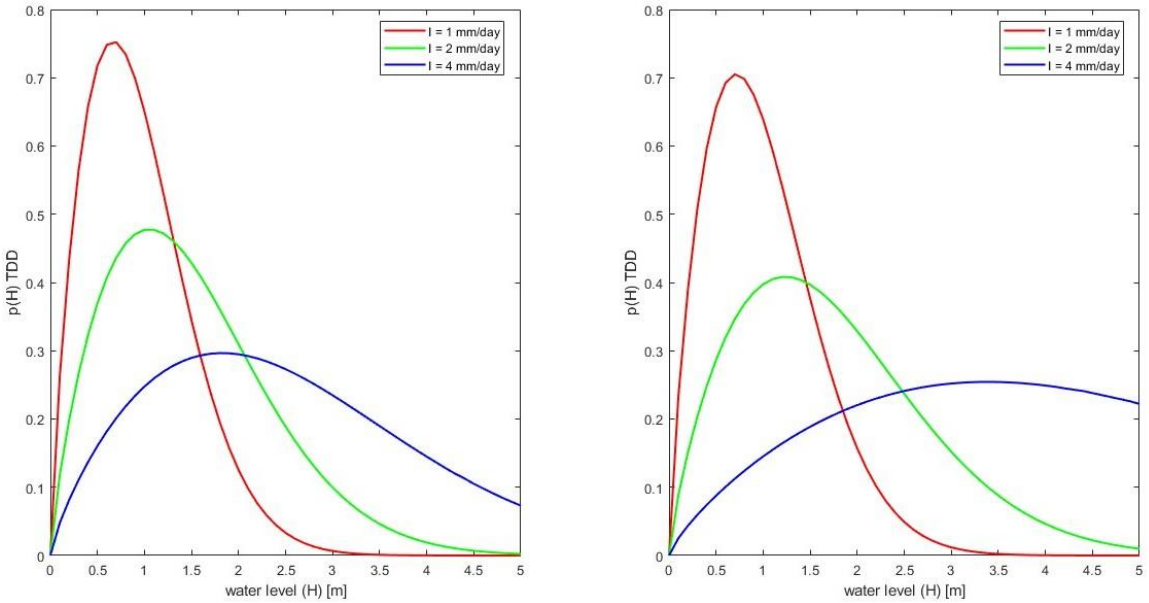

Figure 4: Theoretically derived distribution (TDD) of the water level associated with three values of the mean daily rainfall (red I = 1 mm/day, green I = 2 mm/day, blue I = 4 mm/day) using two different values of the time rate of the Poisson process: 0.1 for the left panel and 0.2 for the right one. All the other parameters are: h_s = 5 m; α = 5000 m^3, β = 1.78, A_b = 10 km^2, φ = 0.5. In addition, the daily withdrawals (L) are assumed to be 30% of the incoming discharge.

In Figure 5, the TDD is reported for two values of the α coefficient of the stage-storage capacity curve of the dam (α = 3000 and 5000 m3) using three different values of the height of the spillway crest, h_s: 3, 5 and 8 m.

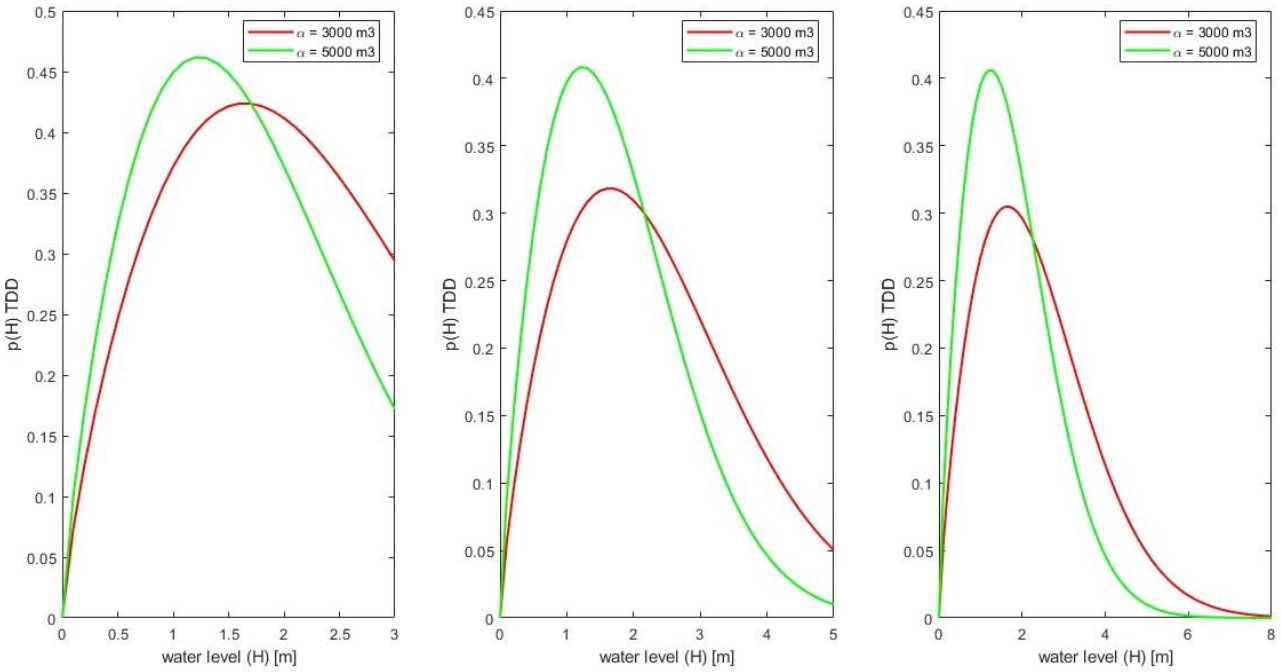

Figure 5: Theoretically derived distribution (TDD) of the water level associated with two values of the coefficient of the stage-storage capacity curve of the dam (α = 3000 and 5000 m^3) using three different values of the height of the spillway crest: 3 m for the left panel, 5 m for the central panel and 8 m for the right one. All the other parameters are: β = 1.78, Ab = 10 km^2, φ = 0.5, Poisson time rate = 0.2, and I = 2 mm/day. In addition, the daily withdrawals (L) are assumed to be 30% of the incoming discharge.

In addition, a numerical hydraulic simulation of the dam operation was carried out using the same rainfall forcing (sequence of instantaneous pulses that occur in a Poisson process of time rate λ) adopted for the proposed TDD. The comparison between the TDD of the water level (continuous blue line) and the empirical probability

density function (pdf) obtained via numerical hydraulic simulation (dashed red line) helps in understanding the reliability of the proposed methodology and quantifying the impact of the approximations adopted. Results are reported in the following Figure 6.

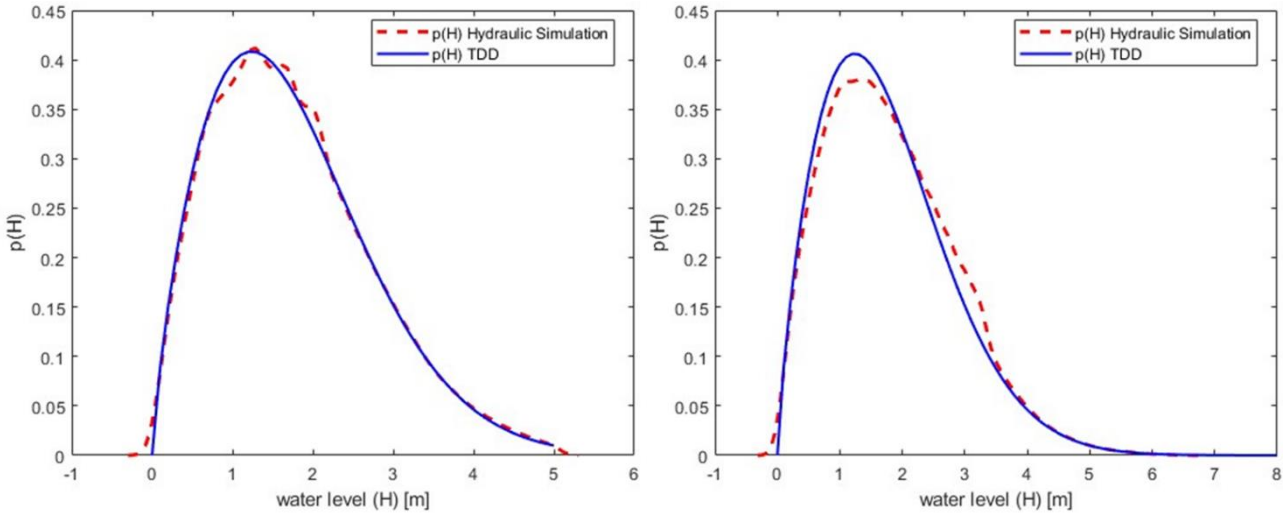

Figure 6: Comparison between the theoretically derived distribution (TDD) of the water level (continuous blue line) and the empirical probability density function (pdf) obtained via numerical hydraulic simulation (dashed red line) for two different values of the height of the spillway crest: 5 m for the left panel and 8 m for the right one.

The numerical simulation was carried out at the daily scale by considering a dam with the following characteristics: h_s = 5 m; α = 5000 m^3, β = 1.78, A_b = 10 km^2, φ = 0.5. In addition, the daily withdrawals (L) are assumed to be 30% of the incoming discharge, while the inflow is modelled as a sequence of instantaneous pulses that occur in a Poisson process of time rate λ = 0.2 and main daily rainfall of 3 mm.

The proposed framework has been applied to a case study in Basilicata Region: the Camastra dam located in Trivigno (Province of Potenza).

According to the 2017 bathymetric survey, the following characteristics of the Camastra dam has been considered: h_s = 21.3 m; α = 85970 m^3, β = 1.7681, A_b = 340.6 km^2, φ = 0.45. In addition, the daily withdrawals (L) are assumed to be 15% of the incoming discharge, while the inflow is modelled as a sequence of instantaneous pulses that occur in a Poisson process of time rate λ = 0.15 and main daily rainfall of 2.5 mm.

The comparison between the theoretically derived distribution of the water level (continuous blue line) and the empirical probability density function (pdf) obtained via numerical hydraulic simulation (dashed red line) for the Camastra dam is displayed in Figure 7. It is important to report that the numerical simulation has been performed in a simplified manner, without considering the complex operational rules that govern the actual dam management.

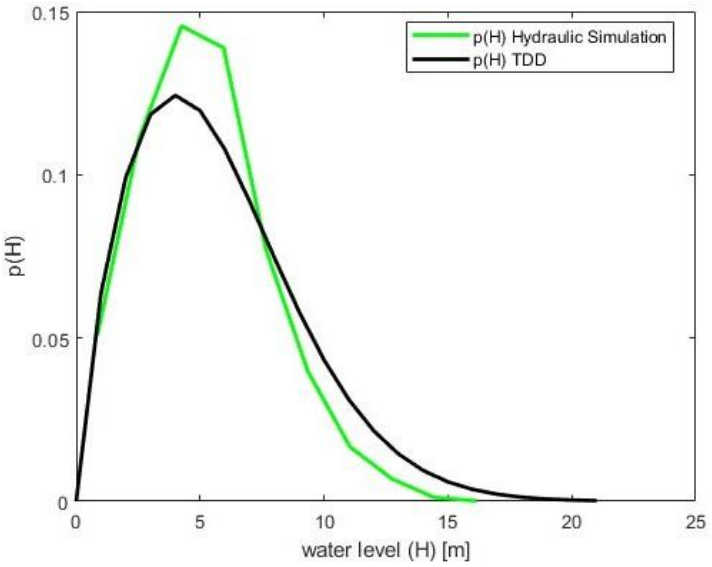

Figure 7: Comparison between the theoretically derived distribution (TDD) of the water level (continuous blue line) and the empirical probability density function (pdf) obtained via numerical hydraulic simulation (dashed red line) for the Camastra dam.

3.2.a.3 Sediment transport model for dam filling prediction

3.2.a.3.1 SMART-SED application to the Camastra catchment

The SMART-SED model was applied to a case study in the Basilicata region, focusing on the Camastra Dam located in Trivigno municipality (Province of Potenza). The dam lies in a valley encompassing the municipalities of Trivigno, Anzi, Laurenzana, and Albano di Lucania, where it impounds the Camastra River, a tributary of the Basento River. Construction began in 1962 and was completed in 1967. The dam stands 54 meters high and has a storage capacity of approximately 32 million cubic meters. The reservoir serves multiple purposes: it supplies drinking water to the city of Potenza and surrounding areas, provides irrigation water to the Bradano-Metaponto Irrigation Consortium, and delivers industrial water to the city of Matera in the Basento Valley (Cimorelli et al., 2021). The study area corresponds to the Camastra (Cimorelli et al., 2021). The study area corresponds to the Camastra catchment, which covers approximately 342 km², as shown in Figure 8.

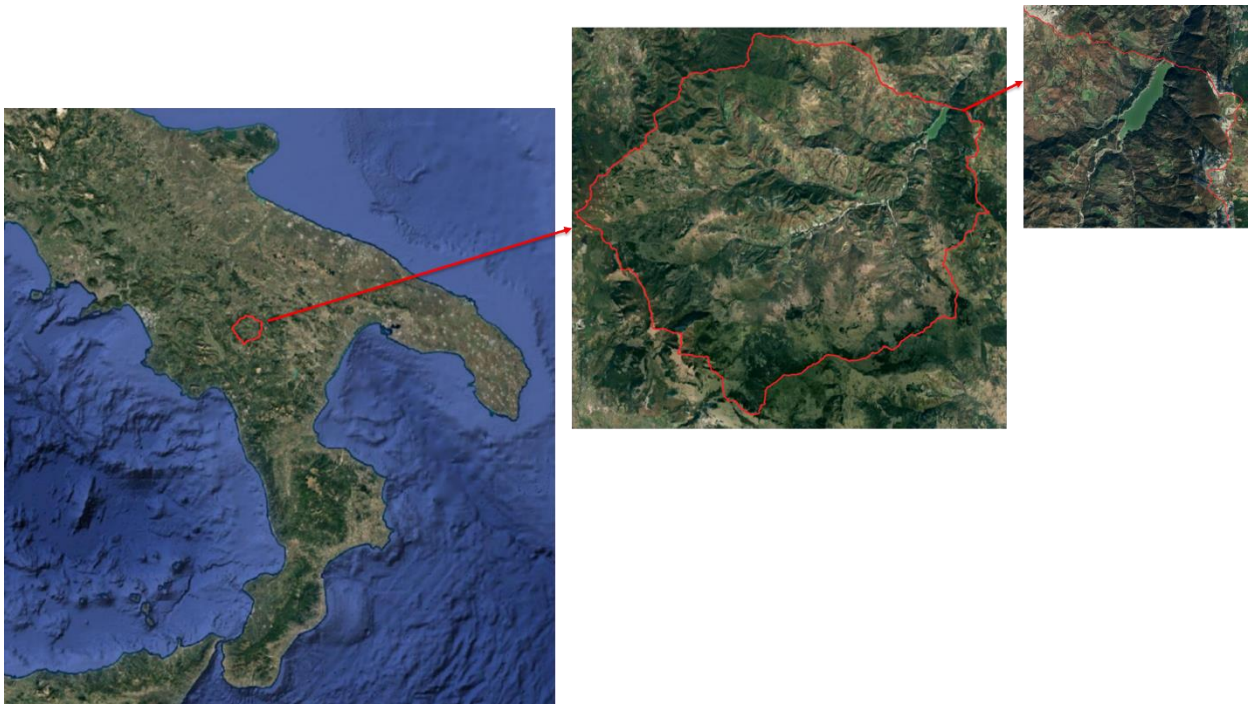

Figure 8: Overview of the Camastra catchment and zoom on the Camastra lake.

As this reservoir plays an important role in regional water supply, sediment accumulation and dynamics within it are specifically investigated by the present PNRR project. In the Camastra Lake, the siltation history has been well documented. Eight bathymetric surveys were conducted over a 25-year period (on average, one every two years between 1993 and 2005), which represents a rather unique dataset in the Italian context. Based on these bathymetric data, it was possible to reconstruct the chronology of sediment deposition within the reservoir. Between 1867 and 1988, the average annual sedimentation rate was estimated at 3.33 x 10^5 m^3/year (Table 1). From 1988 to 1993, this value increased to 1.29 x 106 m3/year due to shallow landslides that occurred along the right bank of the Camastra reservoir (Cimorelli et al., 2021). These landslides were triggered by several rapid reservoir drawdowns that took place between 1988 and 1990, coinciding with the beginning of municipal water supply operations. From 1993 to 1997, the annual average sedimentation rate gradually decreased to its pre-landslide level (3.24 x 105 m3/year), as the slope movements had stabilized by 1993. In the period 1997–2017, the annual average sedimentation rate further declined to the current value of 1.18 x 105 m3/year, thanks to the effectiveness of river training actions and soil conservation practices realized throughout the upstream river network (Molino et al., 2007, 2023). The historical evolution of sedimentation in the Camastra reservoir is summarized in Table 1.

Table 1. Temporal evolution of sedimentation in the Camastra reservoir (SC_0 = storage capacity).

Year	SC_0 (m^3)	Volume sediments (m^3)	Yearly sedimentation rate (m^3/y)	Source
1967	3.5E+07	0	0	(Cimorelli et al., 2021)
1988	2.8E+07	7.0E+06	3.3E+05	(Cimorelli et al., 2021)
1993	2.2E+07	1.3E+07	1.3E+06	(Cimorelli et al., 2021)
1995	2.1E+07	1.4E+07	4.9E+05	(Cimorelli et al., 2021)
1996	2.1E+07	1.5E+07	3.1E+05	(Viparelli, 2004)
1997	2.0E+07	1.5E+07	3.5E+05	(Cimorelli et al., 2021)
1998	2.0E+07	1.5E+07	2.6E+05	(Viparelli, 2004)
1999	2.0E+07	1.6E+07	2.6E+05	(Viparelli, 2004)
2005	1.9E+07	1.6E+07	1.2E+05	(Cimorelli et al., 2021)
2017	1.8E+07	1.8E+07	1.2E+05	(Molino et al., 2023)

From Table 1, considering the last two bathymetric measurements (2005 and 2017), the average annual sedimentation rate is approximately 1.18 x 10^5 m^3/year. Assuming that similar erosion conditions persisted

between 2017 and 2023, the total sediment volume accumulated by 2023 can be estimated at 1.84 x 10^7 m^3 while the corresponding storage capacity would be approximately 1.68 x 10^7 m^3. These values are hypothetical and cannot be verified, as no bathymetric survey is available for 2023 in the existing record. This means that, in the absence of sediment removal interventions and under the assumption of the same constant annual erosion rate, the reservoir storage would be completely lost within the next 150 years.

From a geological perspective, the Camastra catchment is composed of sedimentary rocks, including limestones, conglomerates, sandstones, mudstones, and turbidites (see Figure 9 for more details). Lithology and clay mineralogy strongly influence the development and morphology of badlands, as bedrock weathering caused by freeze–thaw and wetting–drying cycles is deeper and more intense in parent rocks containing swelling clays. In general, claystones and other calcareous rocks are affected by erosion through mechanical disintegration in the case of clay-rich materials and chemical dissolution, especially via karst processes, in limestones. These processes result in distinctive landscape features and varying degrees of geological stability across the catchment.

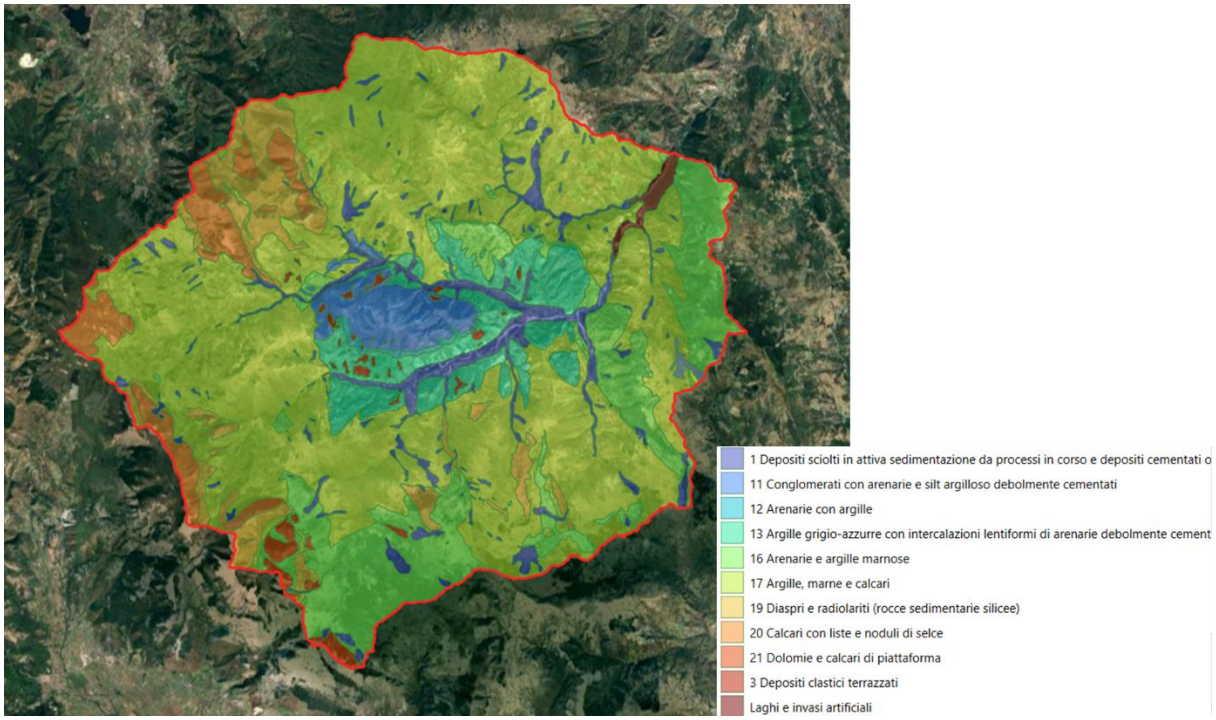

Figure 9: Lithologies present in the Camastra catchment.

This distinct geological and geomorphological framework was particularly valuable for assessing the capabilities of SMART-SED. In addition, the area differs slightly from the Alpine pilot case study, where the model was originally developed, not only in its geological and geomorphological setting but also in terms of climate. The climate in Camastra catchment is classified as warm and temperate, typical of inland Mediterranean areas, characterized by hot, dry summers and cold, rainy winters, influenced by its elevation (approximately 500-800 meters a.s.l.). Over the past 25 years, mean annual precipitation recorded by eight pluviometric stations in the catchment surrounding area has ranged from 437 mm (in 2003) to 1150 mm (in 2013), with a mean value of 755 mm between 2000 and 2023 (the location of the stations is shown in Figure 10, and the annual precipitation values are reported in Table 3). The mean annual air temperature in the catchment (Potenza station) is approximately 12-13°C.

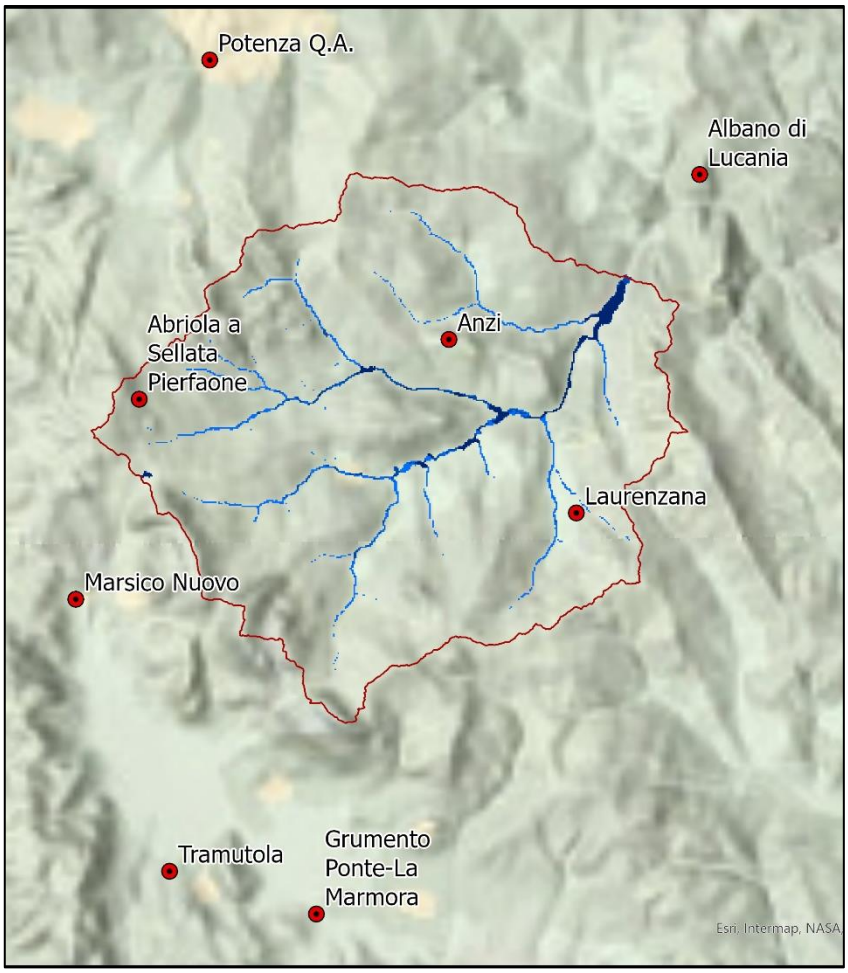

Figure 10: Spatial distribution of pluviometric stations located neare the Camastra catchment.

Table 2. Annual cumulative precipitation values at the Camastra reservoir, derived through IDW interpolation based on data from surrounding pluviometric stations.

Year	Cumulative rainfall (mm)
2000	535.86
2001	495.23
2002	728.05
2003	462.85
2004	801.10
2005	596.27
2006	768.62
2007	652.78
2008	741.61
2009	980.16
2010	1075.80
2011	473.92
2012	812.44
2013	1078.70
2014	737.41
2015	977.02
2016	861.40
2017	564.83
2018	897.86
2019	740.19
2020	722.19
2021	761.43
2022	822.16
2023	837.47

The model was initially applied to the Camastra catchment for calibration purposes, using a resampled version of the TINITALY DEM provided by the INGV institute. The original resolution of 10 m was resampled to a raster cell size of 60 m. Additional input data for the SMART-SED model concerned land use within the catchment area; in this case, the CORINE Land Cover (2018) was considered, as shown in Figure 11.

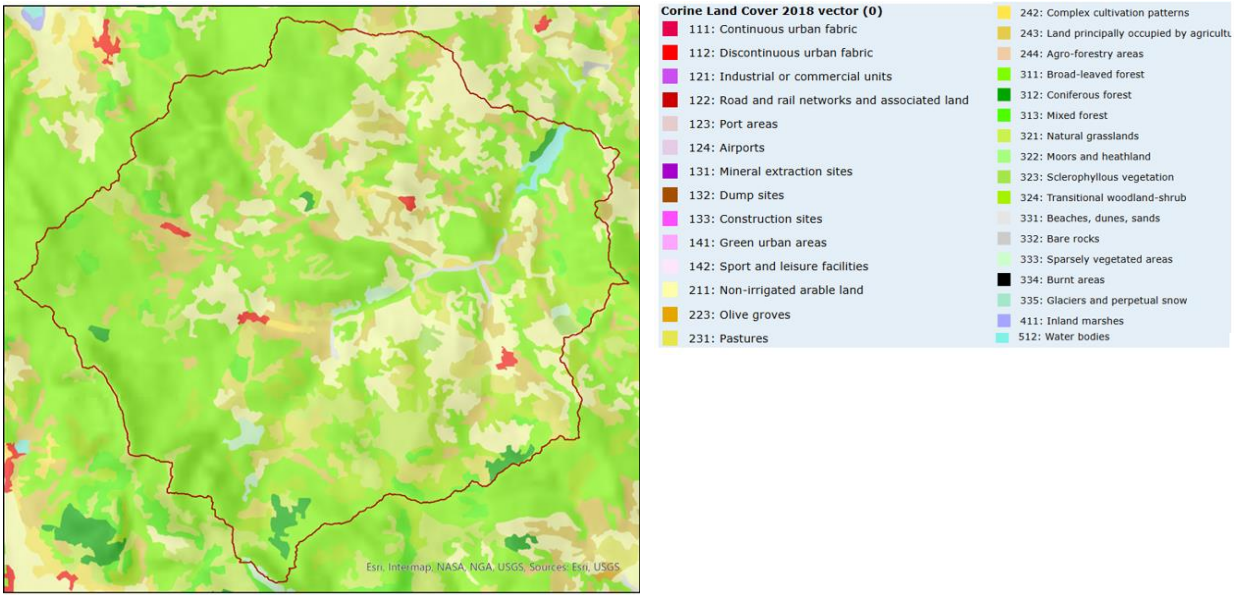

Figure 11: CORINE Land Cover (2018) map of the study area.

The granulometric composition of soil was also included as an input, since the model uses this information to estimate infiltration. The proportions of clay, silt and sand (expressed as percentage value) within the upper 5 meters of the soil were determined using the SoilGrids database. SMART-SED does not require the full particle size distribution of soils across the catchment, as SoilGrids maps are employed solely to estimate infiltration via the SCS Curve Number (SCS-CN) approach (see Gatti et al. (2023) for further information). In this method, the selection of the appropriate Curve Number (CN) value depends on the hydrologic soil group, which is defined based on USDA soil classes and land cover, and is associated with a specific infiltration capacity. Coarser fractions are not required in the implemented infiltration module, as USDA soil classes are defined according to the proportions of sand, silt and clay. Moreover, technically, their absence does not pose a limitation, as they are implicitly accounted for within the hydrologic soil group classification used for CN assignment.

Several yearly scenarios were simulated: 2012, 2013, 2017, 2021 and 2023. The 2013 was chosen as it represents the period with the maximum annual precipitation over the last 20 years, while 2017 corresponds to one of the years with minimum precipitation. The years 2012, 2021 and 2023 were chosen to represent conditions of average annual precipitation.

3.2.a.3.2 Results and discussion

The input parameters described in the previous section, related to geological, geomorphological, and meteorological conditions, were considered in the SMART-SED simulations to reproduce the annual scenarios discussed above. To account for the contribution of the three main streams flowing into the reservoir, ten control points were initially placed within the domain (as shown in Figure 12). This preliminary setup allowed the identification of the most representative simulated points describing the inflow conditions for sediment transport assessment, since the flow velocity distribution along the streams was not known a priori. The analysis indicated that control points no. 1, 5 and 7 and 1, 6 and 8, located at the outlet of the streams entering the reservoir, were the most representative. In contrast, the control points positioned within the lake showed lower flow velocities, which significantly affected the simulated discharge and sediment yield, leading to less reliable results.

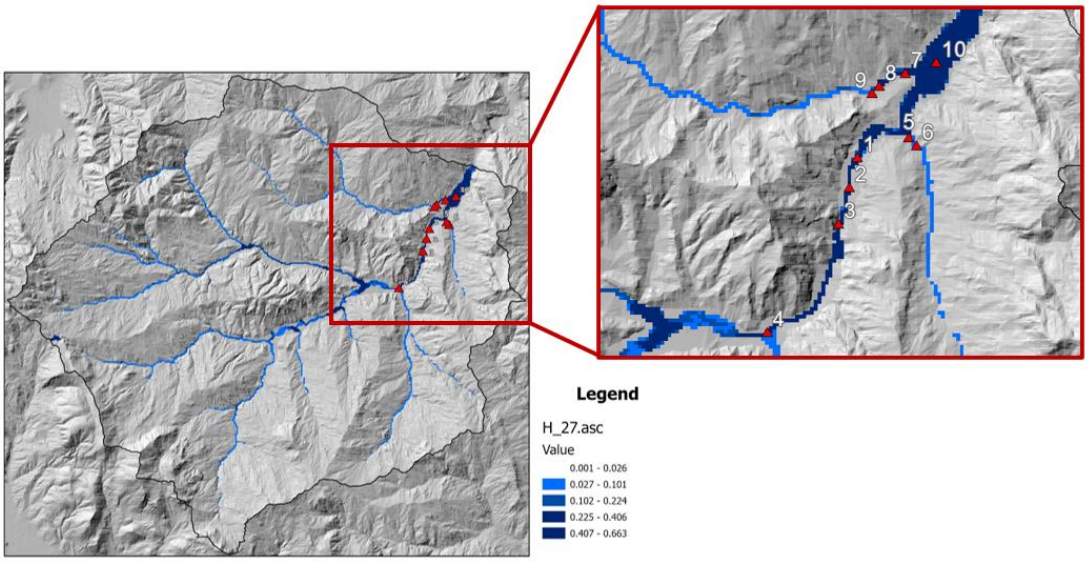

Figure 12: Location of the ten simulated control points, with a focus on the Camastra Lake.

Once the control points were selected, the first outputs of interest provided by the SMART-SED model were the water depth and the discharge across the catchment and at these points over time. Since the amount of precipitation varied among the simulated years, both water discharge and cumulative erosion were estimated for the entire catchment area. For the sake of simplicity, only the discharge results for 2021 are shown in Figure 13 and Figure 14, as this year is representative of average rainfall conditions. The cumulative water volume at the reservoir, obtained by integrating and summing the contributions of the three main streams, is equal to 2.85 x 10^8 m^3.

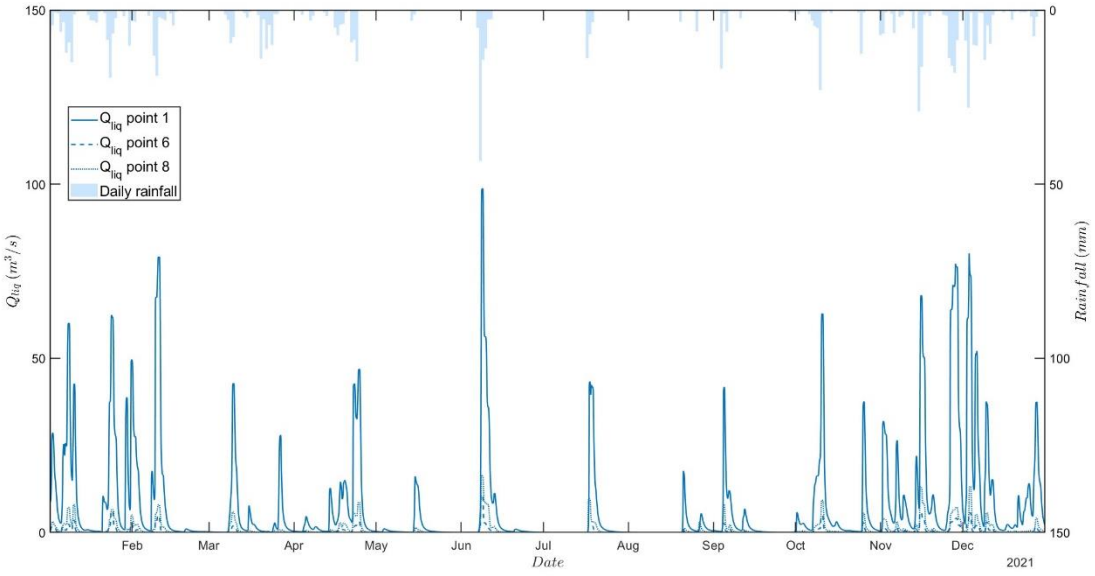

Figure 13: Discharge at control points no.1, 6 and 8, and rainfall at the Camastra dam during 2021.

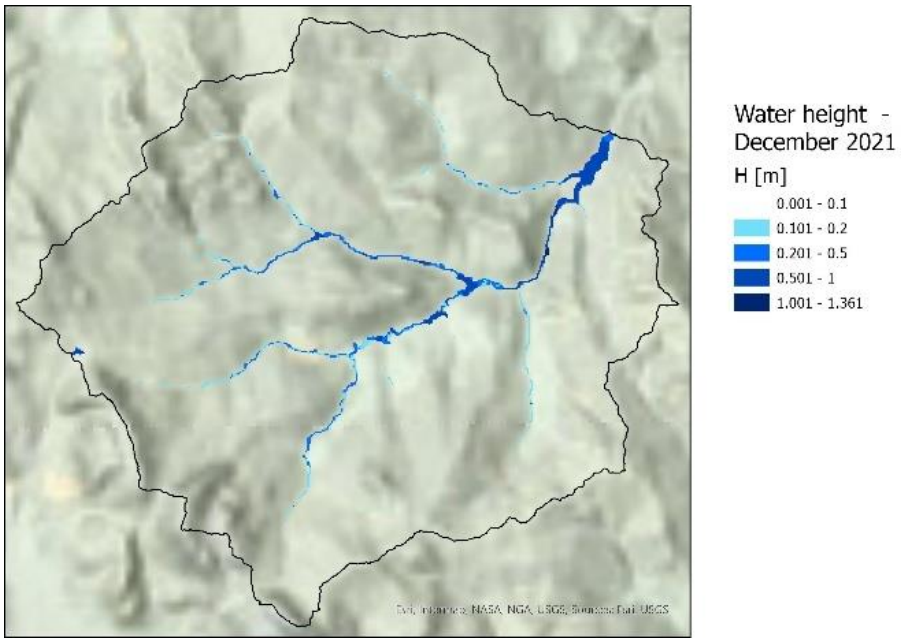

Figure 14: Water depth in the Camastra catchment after a rainfall event in November 2021.

As shown in Figure 13, the discharge at control points 1, 6 and 8 ranges from 0 m^3/s to a maximum of 99 m^3/s, with the peaks corresponding to the timing of rainfall events that occurred during the simulated year. Figure 14 shows the spatial distribution of runoff water depth across the catchment, effectively identifying the drainage system.

The second set of outputs of interest concerns erosion and sediment yield. The sediment volume is obtained by integrating the sediment yield over time. For clarity, only the sediment volume and erosion results for 2021 are presented in Figure 15.

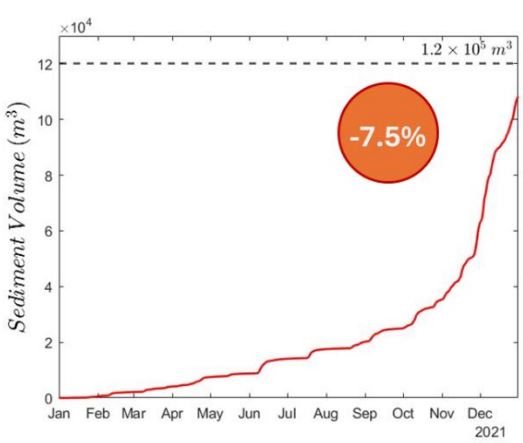

(a)

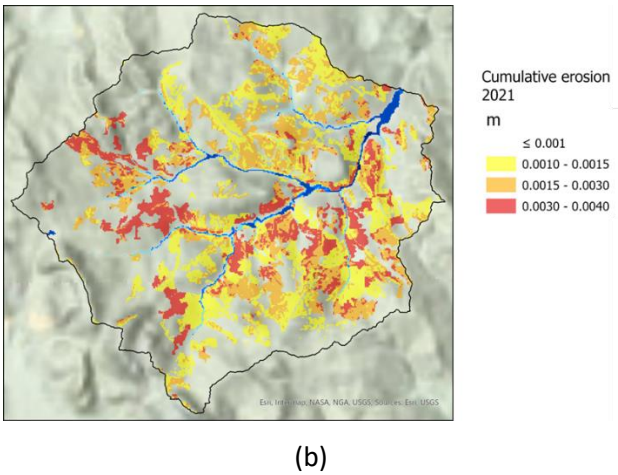

(b)

Figure 15: (a) Total sediment volume estimated as the sum of the contributions of control points 1, 6 and 8 during 2021, compared to the reference value; b) yearly cumulative erosion thickness across the catchment area at the end of 2021.

As shown in Figure 15a, the total sediment volume simulated at control points 1, 6 and 8 reaches 1.02 10^5 m^3 after one year of simulation. Comparing this value with the estimate derived from the bathymetric measurements (1.2 10^5 m^3/year, see Molino et al. (2023)), it appears that SMART-SED underestimates the mean annual sedimentation by approximately 7.5%. Figure 15b illustrates the spatial distribution of sediment erosion across the Camastra catchment, showing that the southern sector of the Camastra Lake is more affected by erosion processes than the northern one.

The total sediments volume simulated in SMART-SED model was then compared to the observed yearly simulation rate to detect the difference in terms of percentage, as shown in Table 3.

Table 3. Annual cumulative erosion in the catchment, sediment volumes at the reservoir and the relative percentage error between simulated and observed values (reference value: 1.2 10^5 m^3) for all simulated years. Cumulative precipitation at the reservoir, estimated using IDW interpolation, is also reported for comparison.

Year	Cumulative precipitation (mm)	Simulated erosion (m3)	Simulated sediment volume (m3)	Error (%)
2012	812	1.8E+05	1.14E+05	-4
2013	1079	3.8E+05	1.96E+05	+78
2017	565	2.2E+05	6.05E+05	-44
2021	761	2.4E+05	1.02E+05	-7.5
2023	838	3.0E+05	1.37E+05	+24

The Table 3 indicates that in years with precipitation close to the 20-year average value (e.g., 2012, 2021 and 2023), the SMART-SED model provides an accurate approximation of sedimentation, with differences from the reference value ranging from -7.5 to +24%. Conversely, in years with extreme precipitation (either maximum or minimum), the model tends to overestimate by up to 78% or underestimate it by up to 44%.

A comparison of annual cumulative erosion across the catchment is shown in Figure 23. It can be observed that the erodible areas are similar between the average rainfall year (2021) and the year with minimum rainfall (2017), whereas erosion is more widespread in the year with maximum rainfall (2013), with an increase in cumulative sediment volume of approximately +60% compared to the average value.

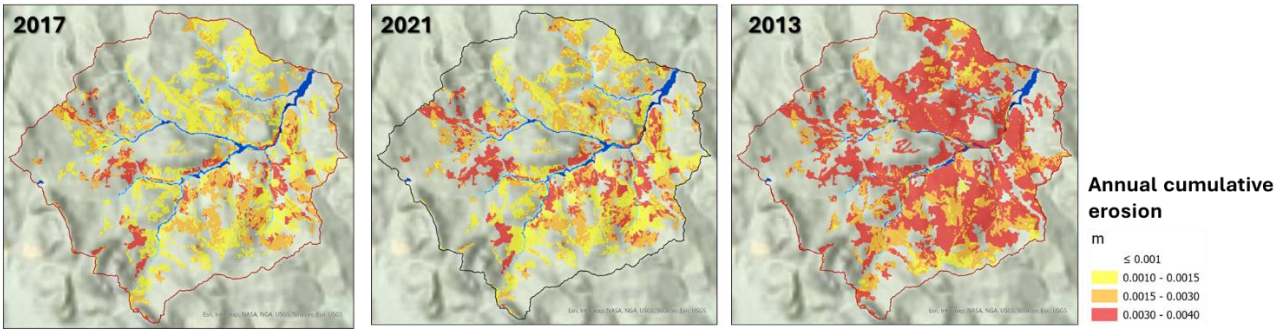

Figure 16: Annual cumulative erosion in the catchment for the years with minimum, average, and maximum rainfall among the simulated periods.

3.2.a.3.3 Results after including landslides phenomena (collaboration with SPOKE VS2)

Since it was observed that the average rainfall year underestimates the mean siltation value, the potential contribution of landslides to the reservoir filling process was evaluated. This aimed to assess whether sediment input from landslide erosion could compensate for the deficit in SMART-SED simulations, which account only for diffuse erosion and do not include channelized or landslide-related sediment transport. As reported in the introductory paragraph, the catchment is characterized by the presence of numerous landslides, as documented in the IFFI, Italian Landslide Inventory (see Figure 17), which are closely related to the bedrock lithology and to the diffused badlands in the area. The most common landslide type is the earth flow, which is typical of such geomorphological settings.

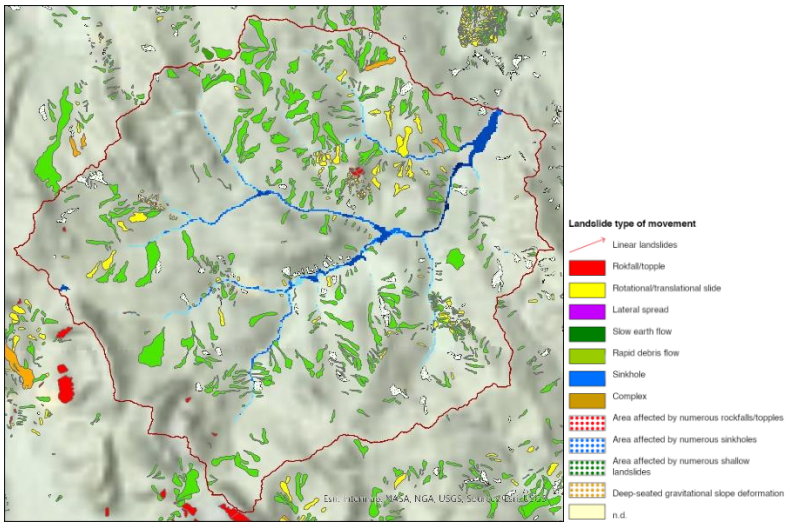

Figure 17: Landslides distribution in the Camastra catchment according to the Italian Landslide Inventory (IFFI).

The contribution of landslides to sediment transport was evaluated by integrating in SMART-SED two types of landslide masks, as shown in Figure 18. The first mask corresponds to the documented landslide polygons from available inventories (IFFI and *PAI, Piano di Assetto Idrogeologico*) and the mapping work by Spoke VS2. The second mask includes the landslide-susceptible areas identified by Spoke VS2 as regions potentially prone to earth-flow type landslides, even if not yet documented. Within the masks, erosion was introduced as parameter independently of lithology or land cover, with elevated erosion values assigned to reflect the high erosive potential of these areas.

This approach allowed the assessment of the potential contribution of latent or undetected landslides to sediment yield, providing an indicative estimate of the maximum sediment erosion and transport volume reaching the reservoir.

Two simulation settings were considered, resulting in a total of four simulations for 2012, a year with average rainfall within the last bathymetry measurement interval. The two simulation approaches were defined as follows:

- Landslide mask treated as a land cover: erosion occurs only within the landslide mask.
- Landslide mask added to the existing land cover (CLC): within the mask, erosion is parameterised at a high value, while outside the mask, erosion is determined based on the land cover and bedrock lithology, as in the simulations described in the previous paragraph.

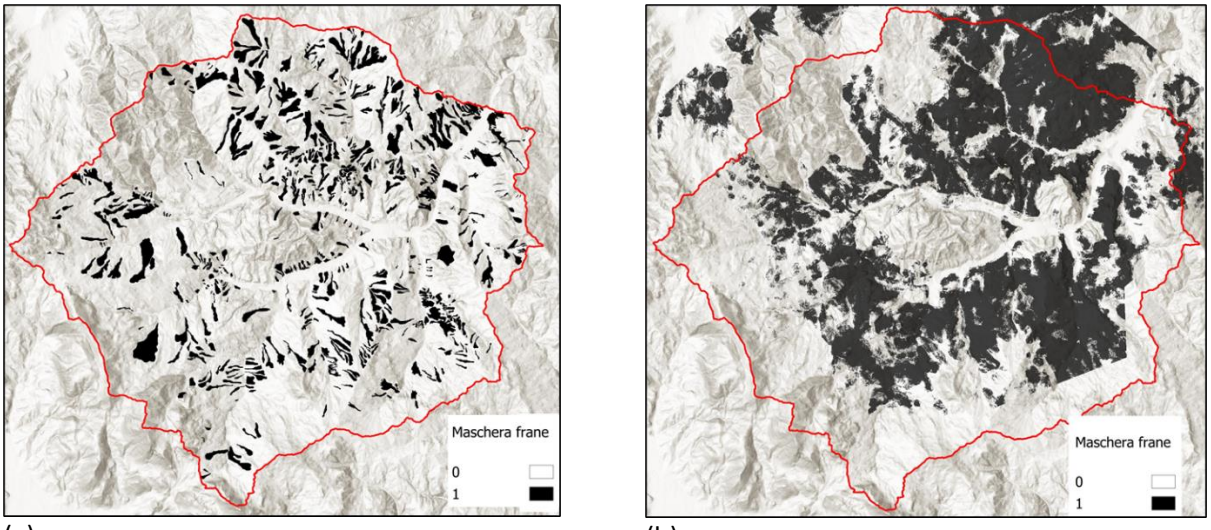

(a) (b)

Figure 18: Landslide masks used in the simulations: (a) landslide polygons, and (b) landslide-susceptibile areas.

In Table 4, Table 5, Figure 19 and Figure 20, a summary of the results obtained from the simulations related to the landslide contribution to erosion and sediment transport is reported.

Starting from the analysis of the 2012 base simulation, it can be observed that about 15% of the total erosion originated from the mapped landslide polygons, even without applying any specific landslide mask. When considering a hypothetical scenario in which all mapped landslides are simultaneously active and characterised by high erodibility, the resulting erosion accounts for approximately 38% of the total 2012 catchment erosion and contributes to about 30% of the mean annual sedimentation in the reservoir, a particularly significant value.

However, when the landslide masks are integrated with the base simulation, so that erosion occurs not only within the landslide areas but also throughout the catchment, no increase in sediment delivery to the reservoir is observed, despite the higher total erosion (+109%). This suggests that not all mapped landslides are hydraulically connected to the drainage network capable of conveying sediments to the reservoir. Moreover, since in the rainiest simulated year (2013) the reservoir siltation increased by +78%, which is significantly higher than the indicative +24% contribution from landslides, it can be inferred that precipitation remains the dominant factor controlling sediment yield.

Regarding the simulations performed using the landslide susceptibility mask, the results show extreme values, representing an upper-limit scenario in which all areas potentially prone to earth-flow type instability are assumed to have the same high erodibility. This condition can therefore be interpreted as a theoretical maximum of both erosion and sediment transport, with a 24% increase in reservoir sedimentation and a 183% increase in total erosion compared to the base simulation. Again, these results confirm that only a fraction of the erodible areas within the catchment contribute effectively to sediment delivery, as many are not connected to the main drainage network.

Table 4. Results of the 2012 simulations assessing the landslide contribution to erosion within the Camastra catchment. The table reports the simulated sedimentation volume at the reservoir and the total erosion volume across the catchment for each mask configuration, comparing the base simulation with those considering erosion only within the landslide polygon and susceptibility masks. Percentages refer to the mean annual sedimentation value (1.2×10^5 m³) and to the total erosion volume of 2012 without landslide masks (1.9×10^5 m³). The value marked with * indicates the erosion of the base simulation occurring exclusively within the mapped landslide polygons.

Mask configuration	Sediment volume [m³]	% of mean annual value	Erosion volume [m3]	% of 2012 erosion volume
No mask	1.1E+05	96	2.8E+04*	15
Landslide polygons	3.5E+04	30	7.3E+04	38
Landslide susceptibility	1.2E+05	102	2.2E+05	113

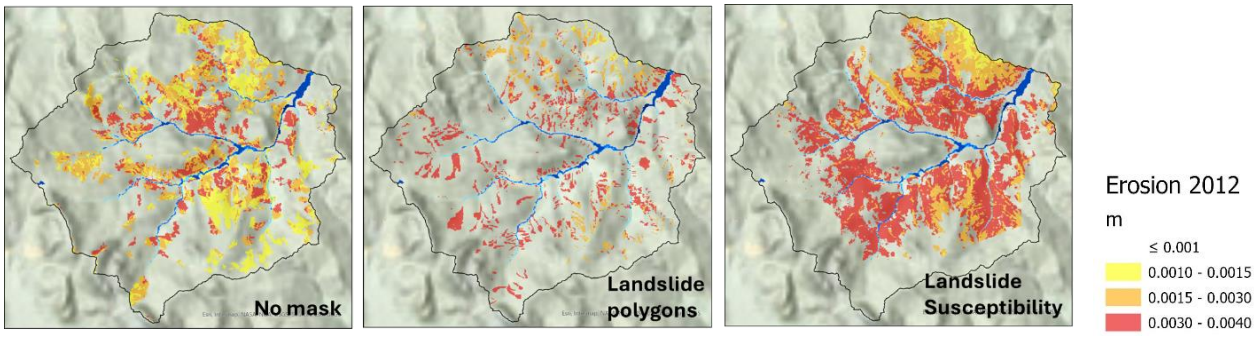

Figure 19: Annual cumulative erosion across the Camastra catchment for the year 2012: (a) base simulation without landslide mask, (b) simulation including the landslide polygon mask, and (c) simulation including the landslide susceptibility mask. In cases (b) and (c), erosion was allowed only within the corresponding masks.

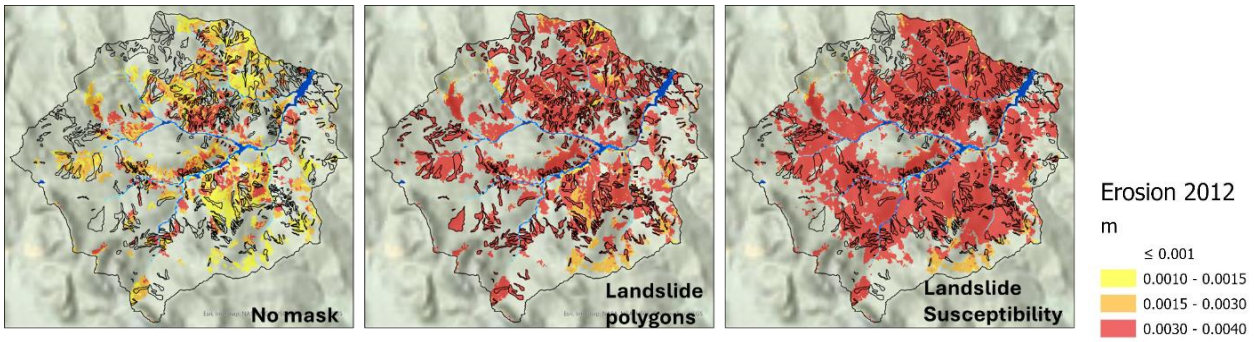

Figure 20: Annual cumulative erosion across the Camastra catchment for the year 2012: (a) base simulation without landslide mask, (b) simulation including the landslide polygon mask, and (c) simulation including the landslide susceptibility mask. In cases (b) and (c), erosion was set to high values within the masks, while outside it depended on land cover and lithology, as in the base simulation.

Table 5. Results of the 2012 simulations assessing the landslide contribution to erosion within the Camastra catchment, considering erosion across the entire basin. Within the landslide masks, a high erosive potential was assigned, while outside the masks erosion was parameterised according to land cover and bedrock lithology, as in the base simulation. The table reports the simulated sedimentation volume at the reservoir and the total erosion volume across the catchment for each mask configuration. Percentages are expressed relative to the mean annual sedimentation value (1.2×10^5 m³) and to the total erosion volume of 2012 without landslide masks (1.9×10^5 m³).

Mask configuration	**Sediment volume [m³]**	**Error [%]**	**Total erosion volume [m³]**	**Erosion increase [%]**
No mask	1.1E+05	-4	1.9E+05	-
Landslide polygons	1.1E+05	-5	4.0E+05	109
Landslide susceptibility	1.4E+05	+24	5.4E+05	183

3.2.a.3.4 Conclusions

The analysis of the simulation outputs confirms that the SMART-SED model is a robust and reliable tool for quantifying hydrological and sediment transport dynamics within the Camastra reservoir catchment. Specifically, the model effectively estimates water discharge rates, identifies sediment source zones, and quantifies sediment volumes mobilized and deposited in the reservoir following precipitation events of varying magnitudes.

The results also highlight the important role of landslides in contributing to sediment yield, particularly in geomorphologically complex areas such as the Camastra catchment. Although SMART-SED currently simulates only diffuse erosion processes, the integration of mass-movement contributions, such as landslides, debris flows, and other gravitational processes, would significantly improve the accuracy of sediment yield estimations. However, even when accounting for the potential contribution of landslides, the simulations show that precipitation remains the dominant factor controlling sediment yield. In fact, during the year with the highest cumulative rainfall (2013), the reservoir siltation increased by +78%, a value substantially higher than the indicative +24% contribution that would result from the activation of all mapped landslides during an average rainfall year (2012).

At present, the reservoir experiences an average annual sedimentation rate of approximately 1.0×10^5 m³/year. In the absence of sediment management or dredging interventions, projections indicate that the reservoir will reach full sediment infill within the next 150 years, effectively rendering it non-functional.

A promising direction for future research involves integrating climate change projections, specifically tailored to the study area, to simulate future rainfall scenarios and assess potential variations in sediment transport volumes under altered meteorological conditions. This would provide valuable insights into the long-term sustainability of the reservoir's storage capacity and support the development of effective mitigation and management strategies.

3.2.b Place-based methodology for territorial vulnerability awareness (Using Geographical Information Systems - GIS)

3.2.b.1 Vulnerability of areas of concern around industrial assets (Seveso Industries) using a multi-hazard and multi-scale approach

3.2.b.1.1 Dataset of industrial assets: Using National Inventory of Major Accident Hazard Establishments.

The current representation of NaTech risks is in general scarce in European countries in the absence of recognized official methodologies for multi-risk analysis with only a few maps overlaying natural and technological hazards (Krausmann et al., 2017). Moreover, finding useful information about such associations at a large scale is never an easy task because the open data are often not accurate, uncertain, or missing in other cases.

In this regard, the data obtained from the Italian national inventory for Major Hazard Industries (MHIs), was used for the spatial representation (ISPRA, 2023). Then, to represent at the national scale the 39 categories of industrial activities previously commented on the "Methodologies Report", were clustered in macro-sectors, using the criteria for classification available in previous research (Casson Moreno et al., 2018; Castro Rodriguez, 2024; Ricci et al., 2021). These criteria were tailored to the MHIs reality where only five to the eight categories of macro-sectors matched with the establishment characteristics. Thus, the macro-sectors categories used were i) chemical and petrochemical, ii) storage and warehousing, iii) power production, iv) bioprocess, and v) manufacturing. In addition, the category of "other" was kept given the fact that in the Italian inventory category 39 "other activity not specified in the list" has 85 plants, which does not allow the classification in macro-sectors.

3.2.b.1.2 Classification of industrial assets according to the principal macro-sectors within the process industry and represented regionally

The frequency of macro-sectors by region was accounted for further representation. Table 6 offers detailed data useful for further discussion, for the 20 Italian regions (names in original language).

Table 6. Establishments frequency by macro-sector, and territorial extension by Italian region.

Characteristics Region	Chemical & Petrochemical	Storage & Warehousing	Manufac-turing	Power Production	Biopro-cesses	Others	Territorial extension (km^2)
Abruzzo	5	8	2	0	0	8	10,832
Basilicata	5	3	0	0	0	2	10,063
Calabria	6	9	2	1	0	0	15,222
Campania	40	21	8	0	0	9	13,671
Emilia-Romagna	43	21	5	0	6	9	22,453
Friuli-Venezia Giulia	11	10	5	0	0	3	7,924
Lazio	17	20	10	0	2	7	17,232
Liguria	6	17	2	0	0	5	5,416
Lombardia	124	58	41	1	1	25	23,864
Marche	7	4	5	0	0	1	9,401
Molise	6	1	0	0	0	0	4,461
Piemonte	40	24	4	0	0	13	25,387
Puglia	10	12	5	1	0	1	19,541
Sardegna	11	13	7	1	0	2	24,100
Sicilia	19	25	2	8	1	5	25,832
Toscana	20	22	8	0	0	5	22,987
Trentino-Alto Adige	2	6	2	0	0	1	13,606
Umbria	3	5	5	0	0	0	8,464
Valle d'Aosta	2	2	1	0	0	0	3,261
Veneto	33	32	20	0	0	3	18,345

Then, the industrial macro-sectors were represented by region at large scale as pie charts. Figure 21 depicts, on a large scale, the distribution of MHIs in Italy clustered in macro-sectors for each region.

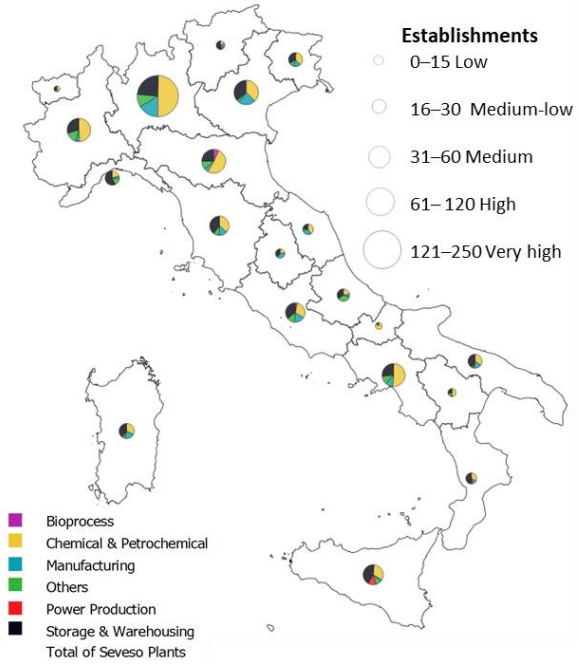

Figure 21: Regional distribution of the industrial macro-sectors for Italian MHIs.

3.2.b.1.3 Geo-localization of Industrial assets as Point-like Infrastructures at large scale (national, regional, provincial) and territorial vulnerability representation.

National-Regional scale.

Then, once industrial attributes are represented at a large scale, their distribution should be associated with meteorological or geophysical information of interest following the function-location approach (refer to the Methodologies Report). To gain a better understanding of the previous idea, the macro-sector regional distribution in Figure 21 should be contrasted with the density of lightning to the ground (Ng in lightning/year·km^2).

Regarding Ng, it indicates the average yearly number of lightning strikes per square kilometer (lightning/year·km2). After CEI Guide 81-3: 1999 – "Average values of the number of lightning strikes on the ground per year and a square kilometer of the municipalities of Italy in alphabetical order"– was repealed in 2014, Ng started to be calculated utilizing nationwide ground lightning location networks (LLS). Geographical coordinates can be used to obtain values of specific locations from the Italian Electrotechnical Committee (CEI) through the online CEI application (CEI ProDis[1]). Although the document regarding the average number of lightning strikes per year and square kilometer in Italian municipalities, that assigned values of Ng to three different areas in Italy as 4, 2.5, or 1.5 lightning/year·km2 respectively (Sabatino & Cordisco, 2013), no longer holds normative status, it can be used as a first approximation to associate lightning territorial vulnerability to MHIs geographical distribution. In addition, the CEI ProDis website application keeps an Italian map visualization for the Ceraunic density of lightning to the ground, divided into three qualitative categories represented by different colors (high-red, medium-green, and low-blue) which can be used to contrast the consistency of discussions hereinafter (Comitato Elettrico Italiano, 2022).

High concern is raised by the greater level of industrialization observed in the northern part of Italy (Ricchiuti et al., 2007), where Lombardy (Lombardia) emerges as the foremost region with 250 establishments, followed by significant contributions from Veneto (88), Emilia-Romagna (84), and Piedmont (Piemonte)

[1] Since Comitato Elettrotecnico Italiano (CEI) has the rights for this italian map, then it can be consulted at https://prodis.ceinorme.it/home.html?sso=y

(81). In the southern part of the country, the prominence of industrialization is noted in the Campania region with 78 establishments. Up to this point, Figure 21 merely offers a visual representation of known data coherent with similar reports (Carpanese et al., 2024). However, it is noteworthy that the pie charts predominantly depict the "Chemical and Petrochemical," "Storage and Warehousing" and "Manufacturing" macro-sectors, with values up to 85% of all critical MHIs in Italy.

Contrasting the information in Figure 21 with the Italian map visualization for the Ceraunic density of lightning to the ground , it is alarming how almost all regions with a high or very high quantity of establishments (except Emilia-Romagna), correspond to zones that contain medium (green), or high (yellow or red) Ng based on the dynamic distribution of colors. On the other hand, there are regions with a medium or medium-low quantity of establishments that fall under zones with significant Ng, such as Friuli-Venezia Giulia, Liguria, or Lazio. It is important to consider both the total number of establishments and their spatial density when correlating meteorological data. The density is influenced by factors such as the geographical extension of the territory of concern or the eventual clustering of establishments in particular zones. For instance, although Liguria has 30 establishments similar to Friuli-Venezia Giulia (29), and both are in a zone with similar Ng color contrasts, the likelihood of a lightning strike affecting one plant in Liguria might be higher than in Friuli-Venezia Giulia, given that the territorial extension where Liguria hosts the 30 MHIs is 0.68 times lower than the Friuli-Venezia Giulia extension.

Moreover, to exemplify an extension of the concepts, but using another perspective of industrial representation and other hazards of interest (geophysical in this case). Then, the representation of MHIs as punctual elements at national levels developed by (Carpanese et al., 2024), has been contrasted with the map of Italian seismic zones according to the level of dangerousness (see Figure 22).

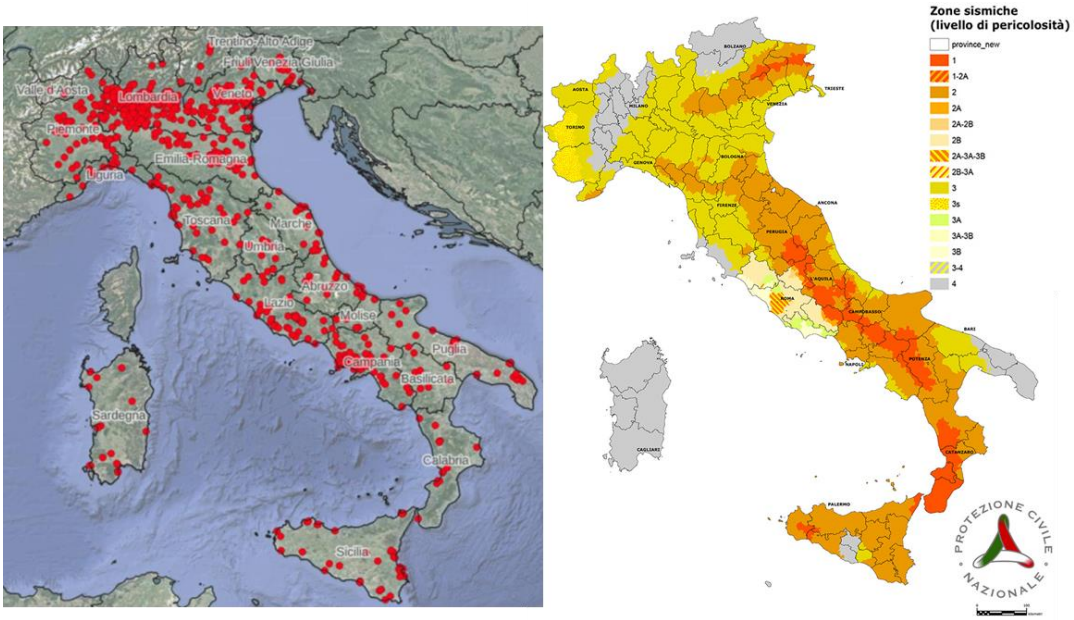

(a) (b)

Figure 22: Association of MHIs with geophysical information of interest information. a) Map of the locations of the Seveso industrial plants in Italy. Source: Carpanese et al. (2024). b) Italian seismic classification. Source: Dipartimento della Protezione Civile (2023).

As was highlighted in previous discussions, the cloud of red points of MHIs in the north of Italy represents more than half of the total Seveso industrial plants in Figure 22a. Comparing the preceding information with Figure 22b, it is evident that despite the high concentration of establishments in the northern regions, just the northeast sector and parts of the central-north correspond to zones with significant levels of hazard (Veneto and portions of Lombardy). In contrast, Piedmont is characterized by a low seismic classification, thus suggesting that the vulnerability of ICIs regarding the location component of the geophysical factor of concern should be lower for this region in comparison with other regions with a high concentration of establishments in the north. Conversely, Campania, which features a high concentration of establishments in the south, corresponds to zones of significant levels of seismic danger. Regardless of the regional density

of establishments, the punctual representation of MHIs allows information to be superposed onto the specific plant location that otherwise would not be taken into consideration. For instance, this facilitates the identification of cases such as plants located in the Molise region, which exhibit diverse seismic classifications alongside the region.

Hence, not only operator technicians should consider these issues to individuate the robustness and mitigation of potential failure modes and scenarios due to seismic factors, but also territorial governments, authorities of the Ministry of the Interior, and other competent authorities.

Since the Function-location approach can be downscaled, subsequently the implementation at the municipal scale of this comprehensive perspective of vulnerability is exemplified.

Regional-Province scale

The Piedmont Region and Turin Province were utilized to show the ICIs vulnerability at regional-provincial scales respectively. The Piedmont Region is in Northwest Italy, and Turin serves as its administrative headquarters. It is Italy second-largest region by extension, seventh in population, and second in number of municipalities. The region is divided into provinces: Alessandria, Asti, Biella, Cuneo, Novara, Vercelli, and Verbano-Cusio-Ossola, as well as the metropolitan city of Turin. Most of the population in Piedmont lives in the plain, mainly in Turin and its surrounding towns. In the past, the region had tremendous growth in production activity. The business expanded rapidly within urban centers without planning regulation, resulting in problems related to the pollution problem inside the urban centers. The automobile sector, which includes the current Stellantis group (formerly FIAT) and related enterprises, is critical to the territorial industry. However, the chemical, food, textile, and garment industries are all essential. The concentration of many industrial activities has caused significant urban congestion, and enterprises are thus concentrated in a limited, heavily populated area (Ferlaino et al., 2015).

In a nutshell, the territorial vulnerability at the scales of interest was represented using open data about both the MHIs and the community around plants. Space-dependent analyses were conducted using geographical information systems (GIS) to produce thematic maps at regional and provincial scales. These maps allocate binding areas around plants which indicate zones of potential damage linked to the classification of stored hazardous substances. These areas differentiate between exclusion and observation zones imposed by policies at the national (D.M. 09/05/2001)[2] and regional levels (D.G.R 26/07/2010 n.17-377)[3]. The resident population was then intersected within the various buffer zones. Finally, it is important to remark that the steps here described, are applicable at medium or punctual industrial scales.

The MHIs were identified as punctual elements on the territory using a dataset provided by the Piedmont Region[4]. These points identify the centroid of the establishments, then it was possible to define the binding areas as buffer zones by extracting, with a selection by location, the polygons of the industrial areas identified by the mosaic of the Piedmont Region[5]. Subsequently, the different exclusion and observation areas were allocated (Castro Rodriguez et al., 2022).

As a result of the differences in the quantity and dangerousness classification of the substances involved in each plant (physical hazards, health hazards, and dangers to the aquatic environment), several final scenarios can be linked (toxic, energetic, environmental pollution). Thus, the establishment of specific thresholds around the establishments is not an easy task. To illustrate diverse scenarios, various thresholds were applied to the facilities according to the Piedmont guidelines (D.G.R 26/07/2010 n.17-377). In particular, the thresholds used were 100 and 300 meters for the exclusion areas and 500, 1000, and 1500 meters for the observation areas.

[2] Ministry of Public Works Decree of May 9, 2001 “Minimum safety requirements in urban and territorial planning for areas affected by establishments at risk of major accidents.” Italian Official Gazette No. 138 16/06/-Ordinary Supplement No. 151

[3] Regional Council Resolution No. 17-377, July 26, 2010, "Approval of Guidelines for Industrial Risk Assessment in Spatial Planning." Official Bulletin of the Piedmont Region No. 31, 05/08/2010.

[4] Regione Piemonte. Dati Piemonte. https://www.dati.piemonte.it/#/home

[5] Piedmont Geoportal https://www.geoportale.piemonte.it/cms

It is important to remark that the place-based methodology here described is compatible with other specific methodologies to determine the safety distances such as the Shortcut Method, described in Annex 6 of M.D. 07/12/2022 Part 1. This expeditious method provides a quick way to define damage and attention zones and estimate the consequences of incidents. It could be particularly useful in situations where minimum data is available or safety reports are insufficient or absent, such as in the case of lower-tier establishments (LTE) which only provide the notification. The principal output of the present subsection is shown in Figure 23.

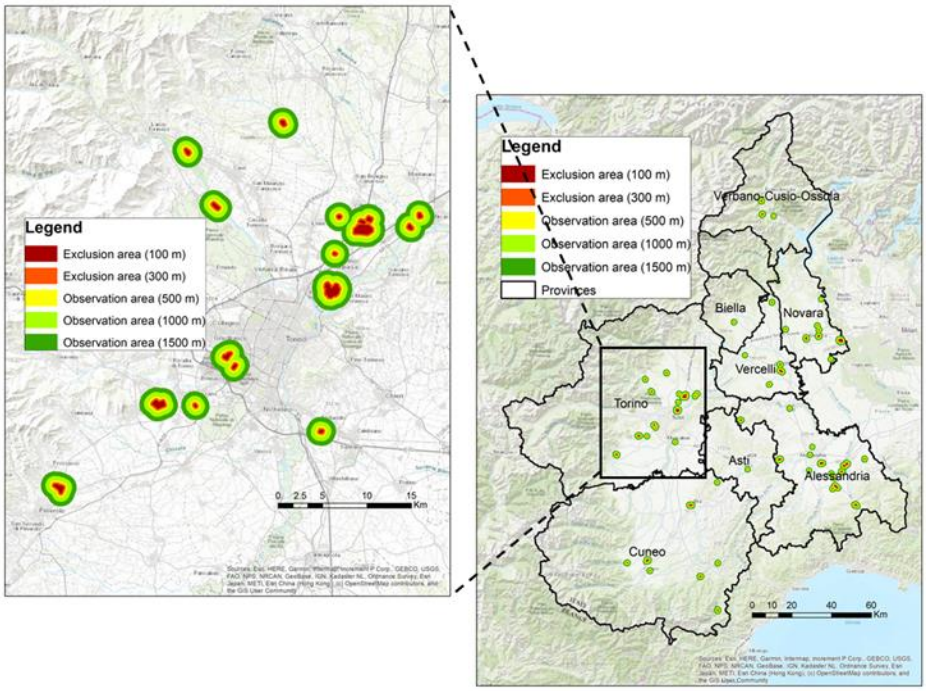

Figure 23: Representation of Seveso establishment and binding areas in Piedmont and Zoom for sector containing the establishments in the Metropolitan City of Turin.

The above illustration represents on its right side, the system of ICIs, which interact with other critical entities for energy, stock, and to provide their products for the development of society within the territory of the Piedmont Region. In parallel, this system corresponds to potentially threatening nodes anchored in the territory. The punctual representation of MHIs enables us to replicate, in major detail, the analysis previously discussed at the national level, relating the ICIs to natural hazards of interest. In addition, the binding area superposition has implications for the identification of potential domino effects for neighboring plants. For instance, moving to the zoomed quadrant within the Metropolitan City of Turin (left side of Figure 23), it can be easily appreciated that areas with a high concentration of establishments have superposed exclusion and/or observation areas. It can be also elucidated how the areas of potential damage can involve municipalities that do not host Seveso plants.

According to the definitions in Annex E of D.lgs.105/15 (Parts 1 and 2), Potential Areas-RIR (Rischio Incidente Rilevante) refers to locations with a high concentration of MHIs that may cause a domino effect. It means that in those areas, at least two domino groups with a distance lower than 1500 m or one domino group with three or more establishments are present. In case of accidents at one plant inside the Area-RIR, it may trigger cascading and escalating events with more severe consequences affecting other neighboring plants or essential infrastructure. Going back to the left side of Figure 23, more than one area of RIR can be identified, through the superposition of the represented potential area of damage. In consequence, as stated in Annex E of D.lgs.105/15, a Safety Study Integrated of Area (SSIA) should be carried out in the Areas-RIR, including mapping tools and thematic charts. Even though some criteria are stated within the text of the legal framework, there are no references to specific methods about how to conduct the SSIA.

After the representation of MHIs as punctual elements and allocation of binding areas, some analyses were introduced, such as the determination of establishment by province and the principal industrial activities developed in the territory (see Figure 24).

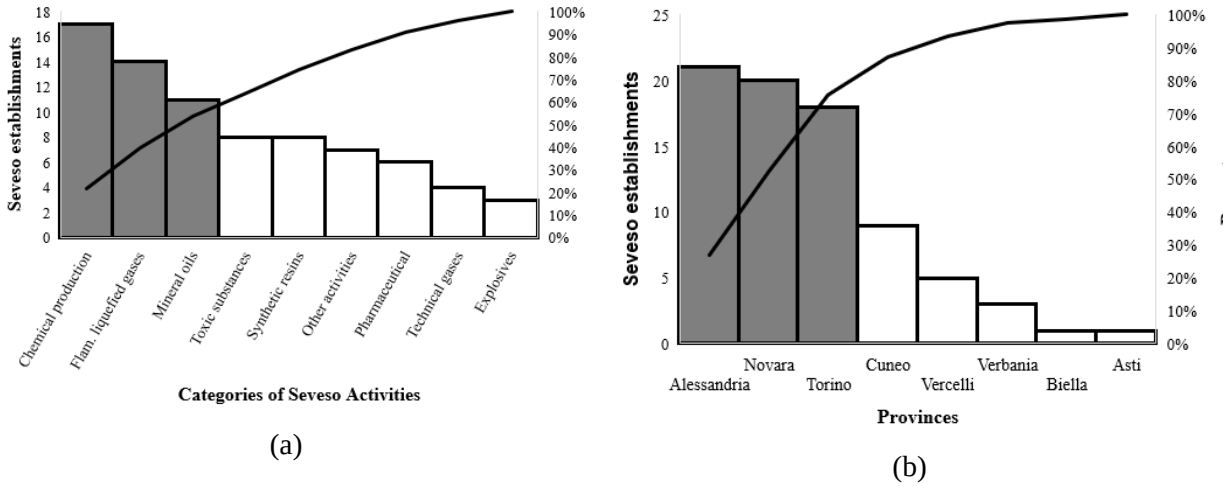

Figure 24: Pareto diagrams: a) Number of Seveso establishments by kind of industrial activities in the Piedmont region. b) Number of Seveso establishments by province in the Piedmont.

Subsequently, to continue connecting functional factors and territorial ones, it was estimated how much population would be affected by the Seveso plants in case of an accident (persons by hectare). Then, the population involved inside the different zones was estimated, considering the intersection of the different used thresholds and the average population density (persons by hectare obtained from the National Institute of Statistics-ISTAT, see Figure 24).

As can be appreciated, the primary or intermediate chemical productions, the storage and the bottling and storage of flammable liquefied gases, and the treatment of mineral oils are the principal three categories (highlighted in Figure 24a) with more than 50 % of the MHIs in the Piedmont Regions. On the other hand, Figure 24b) shows the provinces of Alessandria, Novara, and Torino including more than 75 % of the MHIs in the region.

The density of people in the Seveso exclusion areas (100 to 300 m) in the provinces of Asti, Vercelli, Cuneo, and Verbania (Figure 25) is higher than in other provinces that accumulated more Seveso installations, which shows the large number of people in these provinces who live in the most critical area in case of accidents. Moving to the observation areas used (range of 500 to 1500 m), the same three provinces, Vercelli, Cuneo, and Verbania, are confirmed as more vulnerable for inhabitants in case of accidents, compared to the metropolitan city of Turin.

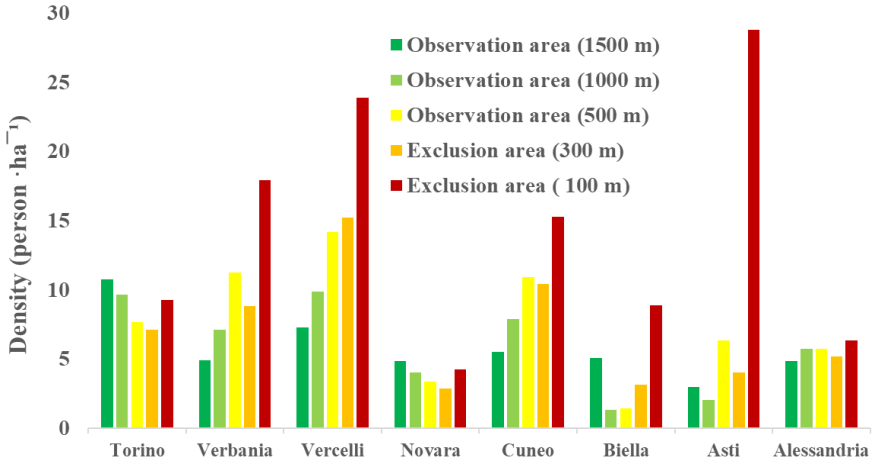

Figure 25: Density of inhabitants (person·ha^{-1}) in the areas of observation and exclusion by province.

The preceding concern suggests potential incompatibilities with the minimum safety criteria regarding land use around Seveso establishments, particularly concerning distances, for the existing plants located in the vulnerable provinces. Although the way to estimate the people potentially affected in case of an accident at the local scale in the D.M. 09/05/2001 presents differences with the spatial method here developed, the latter represents an early way to detect territorial vulnerabilities, which may be used at first glance.

3.2.b.1.4 Contextualization of natural and territorial hazards at the scale of interest (lightning phenomena considered as a pilot study).

Figure 26 shows the macro-sector vulnerabilities contextualization regarding the known records of lightning-triggered NaTech events within the process industry (Castro Rodriguez et al., 2024).

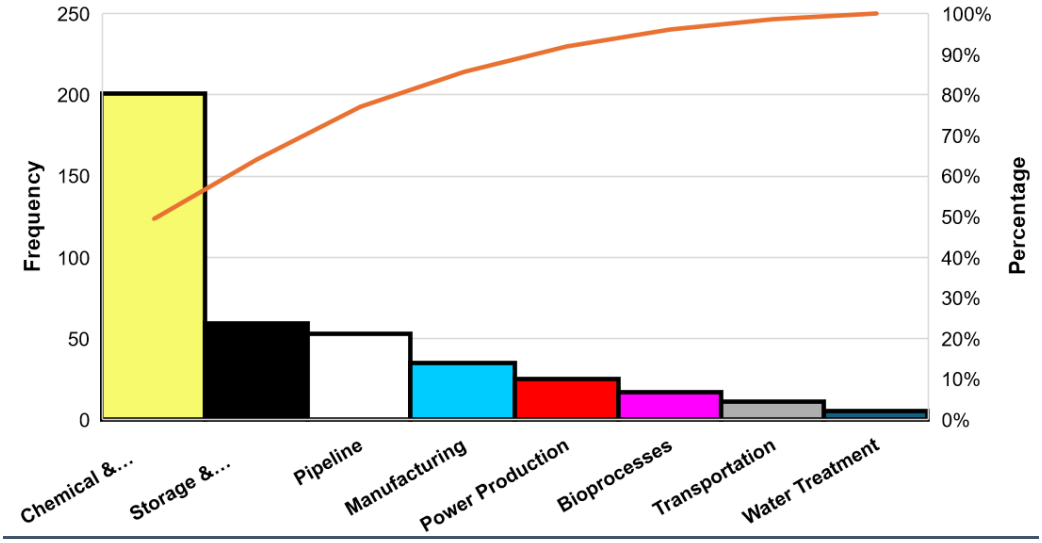

Figure 26: Pareto diagram for macro-sectors vulnerability against lightning strikes within the process industry.

As can be appreciated from Figure 26, the "Chemical & Petrochemical" (yellow) and "Storage and Warehousing" (black) accumulate up to 60% of the registered NaTech events caused by lightning strikes globally in the process industry. Furthermore, if "Manufacturing" (blue) is added, practically 3/4 of the NaTech events triggered by lightning in the process industry are totalized. These categories percentages remain practically identical after the implementation of the Bayesian Networks algorithms to face the uncertainty regarding non-classifiable records. Therefore, there is a clear match between Figure 26 and Figure 21 where the same macro-sector categories correspond with both, the most frequent under the Italian geographical distribution of MHIs, and the most vulnerable against lightning strikes. Since this connection is constated, special should be given to withstand the potential lightning impact on the facilities.

In this line, Table 7 shows the conditional probabilities for categories of vulnerable equipment given the most frequent macro-sectors in Italian MHIs.

Table 7. Conditional probabilities for categories of vulnerability equipment given the most critical macro-sectors within Italian MHIs.

Equipment	Process	Storage equipment	Pipework	Electric & Electronic	Machinery	Flares & Stakes	Other
Chemical & Petrochemical	0.08	0.46	0.03	0.32	0.07	0.02	0.03
Storage & Warehousing	0	0.79	0.02	0.11	0.05	0.01	0.01
Manufacturing	0.02	0.48	0.07	0.28	0.01	0.03	0.11

The information in Table 7 may be useful during the assessment process for the mitigation of the lighting NaTech events on industrial equipment. Despite the three categories of macro-sectors compared, it can be appreciated how "storage equipment" and "electric equipment and electronic devices" comprise the industrial items most susceptible to lightning strikes. In addition, Table 8 shows further interplays between the probabilities of final scenarios for these two critical equipment categories (data from historical analysis).

Table 8. Conditional probabilities for technological scenarios given the failure of the vulnerable equipment against lightning strikes.

Equipment	Fire	Explosion	Release without consequences	Toxic gas dispersion	Environmental contamination	Multiple scenarios
Storage Equipment	0.49	0.05	0.15	0.00	0.13	0.18
Electric & Electronic	0.08	0.01	0.52	0.02	0.32	0.05

As can be appreciated, "fire" is the most probable outcome for storage equipment, 49% of the time, as its energetic charge frequently ignites the stored substances. This finding is consistent with the reported probabilities for ignition resulting from lightning-induced events, as well as the research conducted by Ricci et al. (2021). The same authors highlighted the release with no further consequences (R-NFC) as the most common scenario triggered by all NaTech events, with a general 45%, consistent with the value obtained for the "Electric & Electronic" category (52%). From a phenomenological point of view, often the disruptions caused by these failures are involved in the indirect pathway of the development of NaTech, which means involving utilities or impairments that degrade the system performance or impede the failure mitigation but do not directly impact the dangerous substance.

On the other hand, differences in disaster intensity, territorial density, and natural phenomenon extent can directly affect decision-making at various levels and scales. Since these magnitudes are not registered in most of the recorded events (Krausmann et al., 2011; Reniers et al., 2018), it is difficult to distinguish vulnerability differences between establishments falling under the same macro-sector categories but located in different areas. Thus, whereas functional elements are used for quantitative industrial context evaluations, location considerations are generally disregarded or handled with a qualitative weakness.

For example, when considering only the probabilistic information derived from historical analysis of NaTech incidents caused by lightning, it can be observed that two hypothetical establishments belonging to the "Chemical and Petrochemical" macro-sector, namely Plant A from Liguria (with 30 establishments per region) and Plant B from Apulia (Puglia) (also with 30 establishments per region), are expected to have the same conditional probability of being affected by lightning in any sub-category of "Storage Equipment" (0.46 according to Table 7). However, given that the Ng of Apulia is lower (see Table 6), the likelihood that an establishment in Apulia or Liguria might experience lightning strikes should be different. In addition, the extension of Apulia is 3.6 times higher, and therefore, the density of the number of establishments by territory is lower. Therefore, it is readily apparent that a location factor exists that influences the infrastructural vulnerability assessment against lightning strikes between Plant A and Plant B, depending on their territorial contexts. This issue behaves analogously to other natural factors. Thus, there is a clear necessity to operationalize this "location priority factor" to objectively evaluate the industrial vulnerability against natural hazards and increase its awareness which will be addressed in ongoing activities.

3.2.b.2 Vulnerability assessment of drinking water and wastewater treatment plants as point critical infrastructures using a multi-hazard, multi-scale approach

3.2.b.2.1 Dataset of WWTPs: Using data from Istat, Regione Sicilia and managers of integrated water service (Sicilia)

In order to estimate the effects of extreme events on the critical infrastructures it is certainly important to identify areas and related infrastructures that may be damaged by these events. In this scenario, a multi-hazard approach is a new concept that is becoming commonplace in risk reduction plans. Focusing on individual facilities is an essential starting point for the upgrading and improvement of the facility itself.

Spatial analyses were developed using data on wastewater treatment plants provided by ISTAT (National scale) and Sicilian Region and integrated water service bodies (Regional scale).

Based on ISTAT data (Table 9), a national-scale map was initially created, focusing on the distribution of wastewater treatment plants across various regions, taking into account the number of plants present in each region. Subsequently, at the regional level, the wastewater treatment plants were mapped as point elements, distinguishing them as existing, abandoned, or planned facilities. Focusing on the existing treatment plants, various pieces of information were included in the attribute table, such as capacity and receiving water bodies, which are useful for evaluating the potential consequences in case of a system failure.

Table 9. Number of WWTPs by region (ISTAT, 2015).

Territory	Total
Italia	17897
Nord-ovest	6465
Piemonte	3888
Valle d'Aosta / Vallée d'Aoste	303
Liguria	776
Lombardia	1498
Nord-est	4165
Trentino Alto Adige / Südtirol	235
Provincia Autonoma Bolzano / Bozen	49
Provincia Autonoma Trento	186
Veneto	1148
Friuli-Venezia Giulia	745
Emilia-Romagna	2037
Toscana	1303
Umbria	809
Marche	805
Lazio	635
Sud	2913
Abruzzo	1435
Molise	202
Campania	473
Puglia	189
Basilicata	172
Calabria	442
Isole	802
Sicilia	414
Sardegna	388

A detailed analysis was conducted at a municipal level.

The municipality of Palermo was considered as a case study. Palermo is the biggest city in Sicily, it covers an area of 158 km² and has a population of about 700,000 inhabitants.

The municipality of Palermo is served by two WWTPs: “Acqua dei Corsari” and “Fondo Verde”. The former was completed in its first phase with a capacity of 440,000 population equivalent (PE) and is currently operating at around 375,000 PE, treating the wastewater from South part of the city. Located at an altitude of approximately 7-10 meters above sea level, Acqua dei Corsari WWTP faces challenges primarily due to the fragmentation of the landscape caused by linear infrastructures. The coastal stretch closing the plain is mainly characterized by sandy beaches with a continuous, naturally shaped profile of significant interest.

However, these beaches have not been designated for swimming for a long time. The treated effluent is discharged into the sea through an underwater pipeline located about 1600 meters from the coast. Considering that Acqua dei Corsari WWTP borders the territory of a small town (Villabate), the latter has also been included in the analysis. Fondo Verde WWTP, on the other hand, was designed to serve 105,000 PE and is currently serving about 65,000 PE. Located at an altitude of 20-25 meters above sea level, the surrounding area of the Fondo Verde WWTP includes several key infrastructures, such as roads and railway lines connecting various parts of the city and the surrounding areas. In this case, the treated effluent currently discharges into the sewage system. The plant is being converted into a pre-treatment facility for

incoming effluents and a relay station to the Acqua dei Corsari wastewater treatment plant, including the construction of an emergency discharge pipe.

The municipality of Cefalù was also considered as a case study.

Cefalù is a coastal town in northern Sicily. It covers an area of approximately 65 km² and has a population of around 14,000 inhabitants. The population is growing significantly due to a large number of inhabitants who have moved in and high tourist flows. The municipality of Cefalù is served by two wastewater treatment plants: "Presidiana Sant'Antonio" and "Sant'Ambrogio". The "Presidiana Sant'Antonio" WWTP, located near the coastal area of Cefalù, serves a population equivalent of around 45,000, processing the wastewater from the central and southern parts of the town. Situated at an altitude of about 5-7 meters above sea level, the plant faces challenges related to its proximity to touristic areas and coastal infrastructure, including a coastal road and nearby beaches. Despite its location near the sea, Cefalù's beaches are a focal point for both residents and tourists, with ongoing efforts to ensure their environmental sustainability. The treated effluent from the Presidiana Sant'Antonio WWTP is discharged into the sea through an underwater pipeline extending roughly 800 meters from the coast, minimizing the impact on coastal waters. The nearby port infrastructure adds complexity to the environmental management of this area. The "Sant'Ambrogio" WWTP, on the other hand, is located in the more rural northern part of Cefalù, at an altitude of approximately 25-30 meters above sea level. Designed to serve a population equivalent of around 4,000, it is currently operating at 3,500 PE. The surrounding area is characterized by its natural landscape, including agricultural zones and small settlements. The treated effluent from this plant is discharged into a nearby stream, which eventually flows into the sea.

Figure 27 presents a multi-scale analysis of wastewater treatment plants, offering insights into their distribution and characteristics at different geographic levels. This layered approach enables a comprehensive understanding of the spatial patterns and densities of these facilities, facilitating better-informed management and planning strategies.

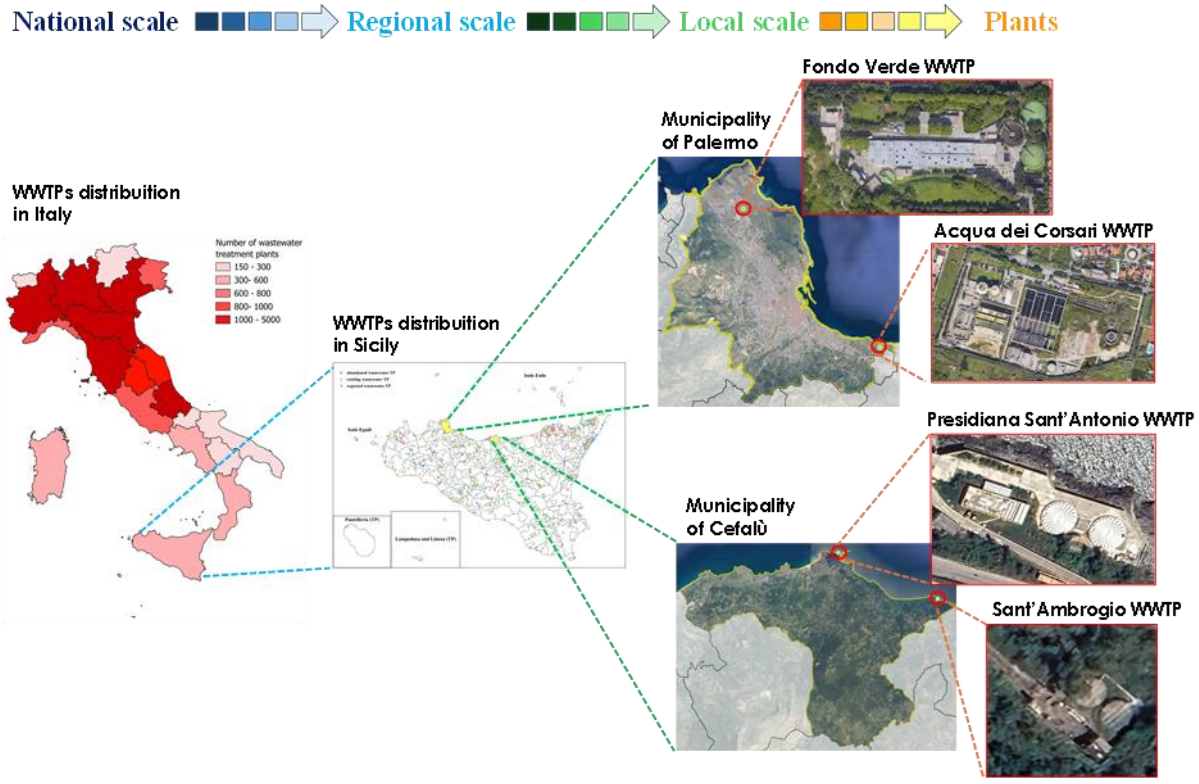

Figure 27: Multi-scale analysis of wastewater treatment plants.

At the national level, the analysis begins by mapping wastewater treatment plants across Italy. The regions are color-coded using a gradient scale to reflect the number of plants in each region. This representation provides a macroscopic view of how these facilities are distributed throughout the country, highlighting areas with higher concentrations of wastewater infrastructure.

Zooming in to the regional level, the focus shifts specifically to Sicily, where the distribution of wastewater treatment plants is represented with greater detail. This regional mapping captures the locations of individual facilities, providing insight into their spatial distribution relative to the geographic, environmental, and demographic characteristics of the territory.

Finally, the study narrows its scope to examine two municipalities within Sicily - Palermo and Cefalù - as case studies. This localized analysis highlights the specific wastewater treatment plants serving these areas, offering a detailed view of their locations. Each facility is analyzed in the context of its immediate environment, including predominant hazards, accessibility, and integration within the municipal infrastructure network. The local-scale analysis is essential for understanding the unique challenges and opportunities associated with wastewater treatment in these municipalities.

The multi-scale approach illustrates the versatility of this methodology in addressing wastewater management challenges. By combining national, regional, and local perspectives, the analysis not only highlights patterns of infrastructure distribution but also identifies specific areas for targeted intervention and resilience-building efforts. This comprehensive framework ensures that strategies can be tailored effectively to the needs of each scale, from overarching policies to local operational improvements.

3.2.b.2.2 Dataset of DWTPs: Using data from managers of integrated water service (Sicilia)

On the other hand, drinking water treatment plants play a crucial role in ensuring a safe supply of drinking water for both the population and various industrial and agricultural activities. These plants treat water from multiple sources, including artificial reservoirs and natural springs, to make it suitable for human consumption. Table 10 shows drinking water treatment plants in Sicilian territory with brief description.

Table 10. DWTPs in Sicily.

Cicala	The Cicala water treatment plant is located in the province of Enna, at an altitude of about 600 meters above sea level. It treats water from the Cicala reservoir and serves municipalities such as Enna, Calascibetta, and other smaller towns.
Risalaimi	Located in Monreale, the Risalaimi plant is at an altitude of approximately 300 meters above sea level. It treats water from the Piana degli Albanesi reservoir and serves a wide area in the Metropolitan City of Palermo, including Piana degli Albanesi and parts of Palermo itself.
Imera	The Imera water treatment plant is located at about 150 meters above sea level near the Rosamarina reservoir in the province of Palermo. It serves the city of Termini Imerese and surrounding areas
Gabriele	This plant is located at an altitude of approximately 450 meters above sea level near Lake Pozzillo in the province of Enna. It supplies water to a large inland area, including towns like Troina, Agira, and Gagliano Castelferrato.
Fanaco	The Fanaco plant is situated at an altitude of about 400 meters in the province of Caltanissetta. It treats water from the Fanaco reservoir and serves cities like Caltanissetta, Agrigento, and nearby towns.
Blufi	This plant is located at an altitude of around 550 meters in the Madonie mountains, in the province of Palermo. It supplies water to small mountain towns such as Blufi, Gangi, Petralia Soprana, and Petralia Sottana.
Ancipa	The Ancipa plant, situated at an altitude of around 800 meters above sea level, is one of the highest in Sicily and treats water from the Ancipa reservoir. It serves mountainous and hilly areas in the provinces of Enna and Messina, such as Troina, Leonforte, and Nicosia
Sambuca	The Sambuca water treatment plant is located at an altitude of approximately 300 meters above sea level near Lake Arancio, in the province of Agrigento. It serves towns like Sambuca di Sicilia, Sciacca, and Menfi.
Acquedotto Rurale Santa Rosalia	This plant is situated at about 500 meters above sea level in the province of Agrigento. It primarily serves the surrounding rural areas and small agricultural settlements.
Santo Stefano di Quisquina	Located at an altitude of approximately 730 meters, this plant is situated in the mountains of the Agrigento province. It provides water to towns like Santo Stefano di Quisquina, Bivona, and Alessandria della Rocca.
Gela	The Gela water treatment plant is located at an altitude of around 50 meters above sea level, near the southern coast of Sicily. It treats water from the Gela River and serves the city of Gela, as well as the nearby industrial and port areas.

In summary, these water treatment plants are located at various altitudes across Sicily, from mountain regions to coastal areas. Each plant plays a crucial role in ensuring a stable and safe water supply in an island region that faces significant challenges due to hot climates and the variability of natural water resources.

3.2.b.2.3 WWTPs and DWTPs mapping using a multi-hazard multi-scale approach

Figure 28 shows the multi-hazard index map crossed with the wastewater treatment plants in the Sicilian territory, with a specific focus on the municipalities of Palermo and Cefalù, and subsequently on their respective facilities. The pie chart and the corresponding table show the number of wastewater treatment plants falling into each category. It can be observed that most of the plants are located in an area where the index assumes a medium-high value.

The tables in Figure 28 present the value of the indicators that make up the indices, thus showing the predominant hazard in the analyzed areas.

It can be observed that for the municipality of Palermo, both facilities are located in areas where the predominant hazard is seismic. In the case of the municipality of Cefalù, it can be noted that for the Presidiana Sant'Antonio wastewater treatment plant, the predominant hazard is geomorphological, followed by seismic hazards, while for Sant'Ambrogio, it is the opposite. This approach allows for the quick identification of key drivers of vulnerability. However, it is essential to proceed with a detailed multi-level analysis, examining individual maps and the spatial distribution of factors, to gain a more comprehensive understanding and inform targeted interventions.

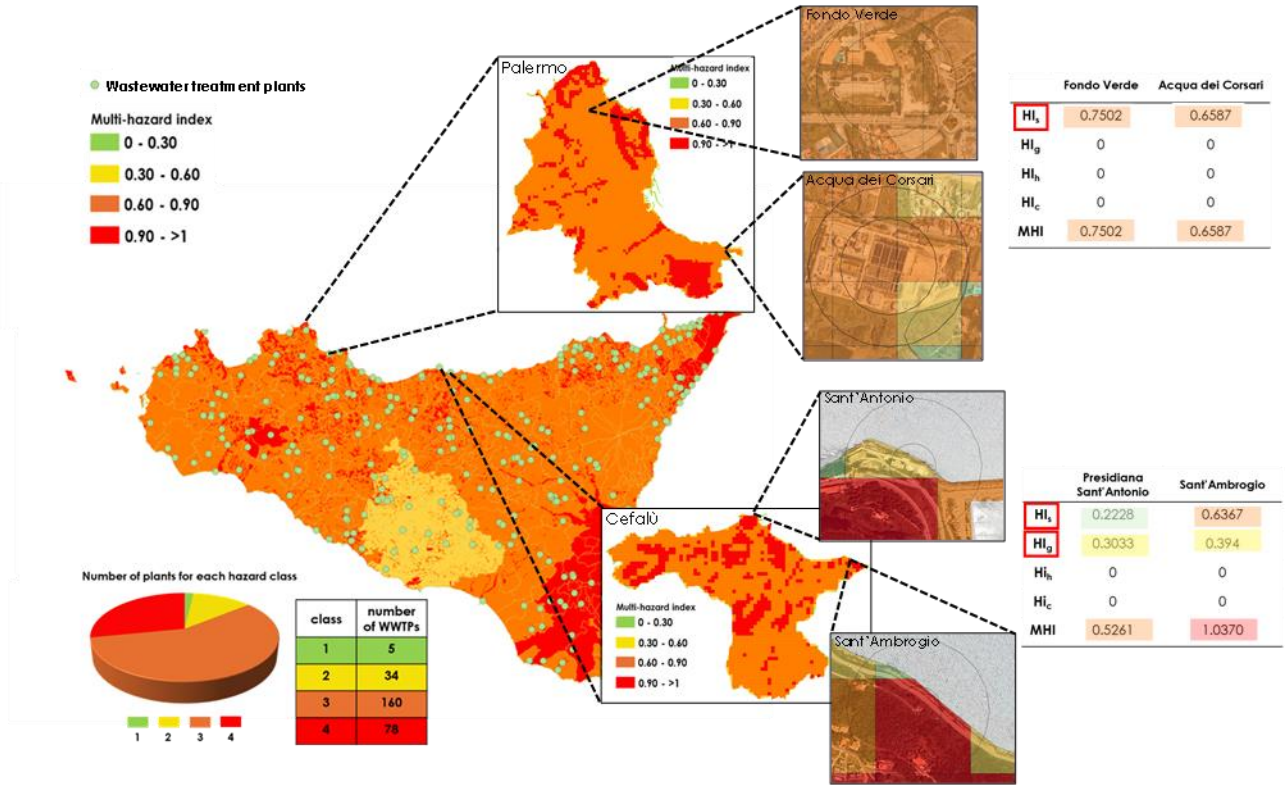

Figure 28: Results from the multi-hazard approach depicting vulnerability between WWTPs and Territory.

A similar approach was adopted for the analysis of drinking water treatment plants (Figure 29). The same multi-hazard index map was overlaid with the locations of drinking water treatment facilities across the Sicilian territory, enabling a detailed assessment of their exposure to various hazards. The methodology used was the same as that applied to the wastewater treatment plants, ensuring consistency in the analysis process.

The overlay of the map with the water treatment facilities allowed for the classification of these infrastructures into the four hazard categories defined by the multi-hazard index. This facilitated an understanding of the overall risk distribution affecting water treatment facilities and highlighted the most critical areas. A pie chart and a corresponding table were created to represent the number of facilities in each hazard category, providing a clear visualization of the findings.

The analysis revealed that, as with WWTPs, a significant portion of DWTPs is located in areas with a medium-high hazard index. This emphasizes the widespread exposure of critical water infrastructure to multiple hazards, highlighting the importance of integrated risk management strategies.

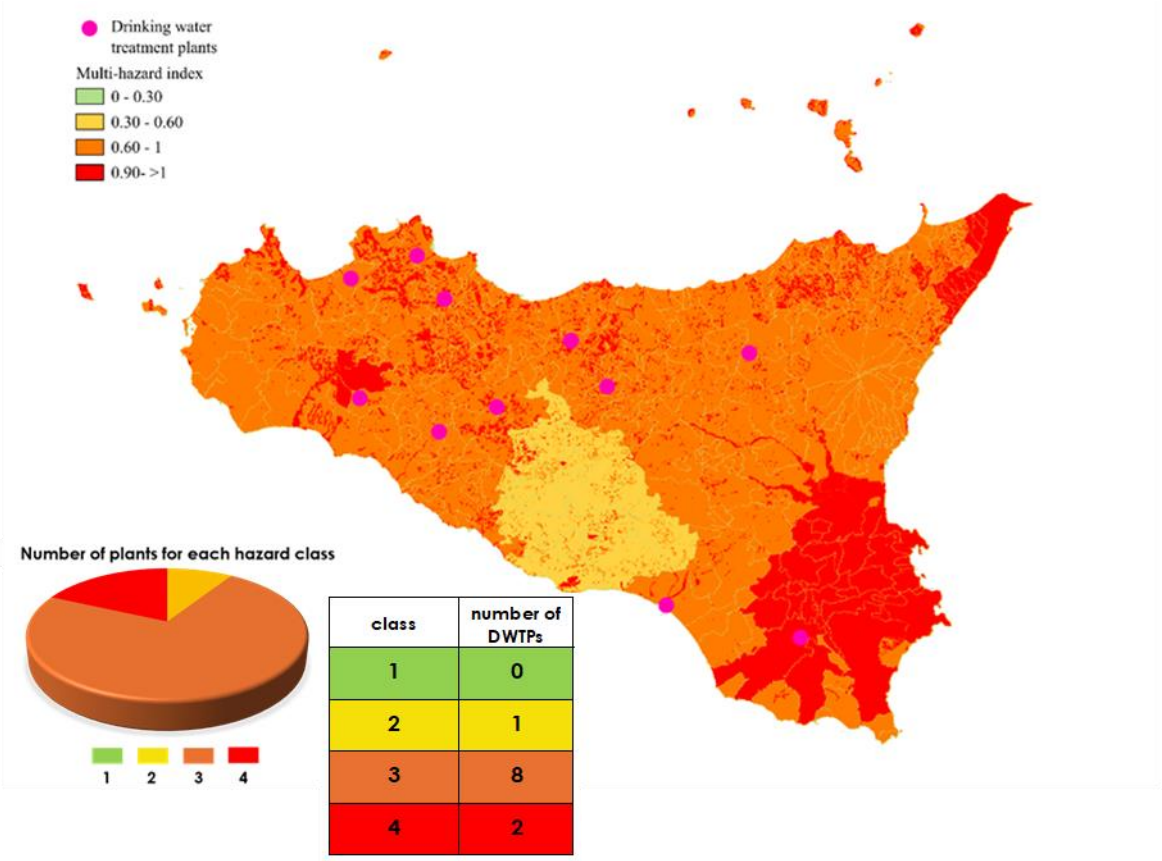

class	number of DWTPs
1	0
2	1
3	8
4	2

Figure 29: Results from the multi-hazard approach depicting vulnerability between DWTPs and Territory.

3.2.b.3 Conclusions

The implementation of the Function-Location approach allowed the representation of technical attributes belonging to the Major Hazard Industries (MHIs) associated with meteorological or geophysical information of interest. Lightning density on the ground was utilized to establish connections between industrial macro-sectors and regional distribution. Notably, regions with a high concentration of establishments often coincide with areas experiencing medium to high lightning density. Moreover, the most prevalent macro-sectors within Italian geographies, such as Chemical and Petrochemical, Storage and Warehousing, and Manufacturing, were found in precedence to be particularly vulnerable to lightning strikes.

The representation of Major Hazard Industries (MHIs) as punctual elements, contrasted with meteorological or geophysical data at a large scale, facilitates case-by-case identification. Moreover, the development of a place-based procedure to establish safety distances, delineating exclusion, and observation areas around MHIs as buffer zones, proves invaluable. This procedure assists in the identification of areas with high concentrations of establishments, where overlapping safety distances with neighboring plants highlight potential implications for domino effects and enable the estimation of inhabitants in accident-prone areas. It also offers a swift and direct way to detect incompatibilities between existing or new establishments and minimum safety criteria for land use around Seveso sites, thus serving as an early detection system for territorial vulnerabilities.

The developed multi-hazard approach significantly impacts the assessment and management of hazards for water treatment plants, addressing several existing gaps in the literature. Traditionally, these plants have been evaluated for individual hazards separately, without considering the interaction between them. A challenge associated with the multi-hazard approach is that, while various assessment methods are known

for the "single-hazard" approach, there are few studies on the application of the multi-hazard approach (Kappes et al., 2012). However, the current approach will be further improved by considering the mutual interactions of the various hazards and assigning different weights (Tilloy et al., 2019).

This tool contributes to increase awareness of territorial vulnerability based on spatial analysis. Moreover, it allows considering the combined effect of different hazards to be analysed according to a holistic approach, so as many hazards can be added. The subsequent identification of possible equipment failures triggered by a natural event, and its potential consequences, can suggest to WWTP managers the correction measures to adopt in order to increase the resilience of the infrastructure.

3.2.c Coastal flooding caused by tsunami waves generated by earthquakes

3.2.c.1 Introduction

The methodology described in the "DV6.3.2 Methodology Report" was applied hereinafter to the Messina Strait through a hazard assessment example and published in a scientific paper (Ruffini et al., 2026) accepted and in the process of being published online where a more complete description of the methodology and the application was included. This application will focus on the Messina Strait and specifically on the three areas of Villa San Giovanni, Messina, and Reggio Calabria, due to these being the three most densely populated areas of the Messina Strait. This application allows to also further compare the results derived by applying this methodology to the simplified inundation maps from ISPRA.

3.2.c.2 Input data and numerical setup

The numerical grids presented in the following section were obtained through the interpolation of three merged datasets. For the emerged areas of both Calabria and Sicily, the Digital Terrain Model (DTM) derived from the 2008 survey conducted by the Italian Ministry of Environment and Energy Security (Ministero dell'Ambiente e della Sicurezza Energetica – MASE) was employed, available upon request at https://gn.mase.gov.it/portale/home. This dataset, featuring a 2 × 2 m spatial resolution, was chosen for its ability to accurately represent coastal morphology. For the nearshore bathymetry, nautical charts were utilized, particularly in the proximity of the areas of interest, to provide a detailed description of the harbour zones. Offshore, the bathymetric dataset was taken from the European Marine Observation and Data Network (EMODnet Bathymetry Consortium, 2022) with a resolution of 100 m in a UTM coordinate system. The final merged dataset, interpolated over the computational grid employed in the inundation simulations, is shown in Figure 30.

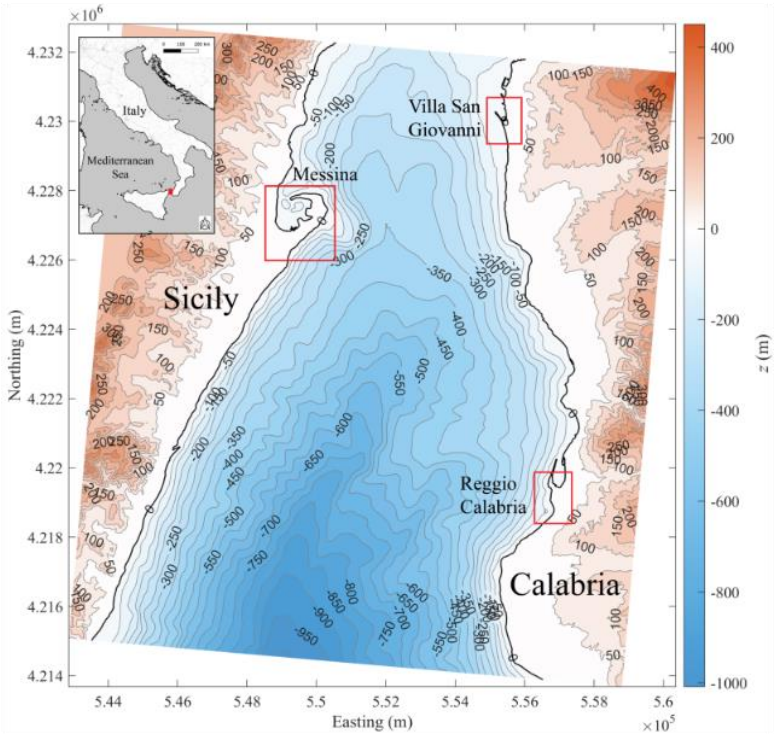

Figure 30: Bathymetry and topography of the area used for the inundation simulations.

3.2.c.2.1 Boundary conditions and numerical grids for step II and step III

Simulations for both steps were carried out using the numerical model described in "DV6.3.2 Methodology Report". In the second step, quasi-2DV simulations, referred to as "quasi" due to the layer-based

formulation of the SWASH model, were performed along the transects shown in Figure 31 (t1–POI 4 and t1–t2, indicated by yellow lines). A spatial resolution of 100 m was adopted, corresponding to more than two orders of magnitude smaller than the tsunami wavelength. At the offshore boundary, a weakly reflective condition was imposed, with the surface elevation time series derived from the N-WAVE theory serving as input. To avoid wave reflection at the downwave boundary, a sponge layer coupled with a constant-depth plateau was implemented, ensuring that only the incident tsunami signal was retained within the computational domain. For each wave condition, the sponge layer was sufficiently extended to suppress any residual reflection from the downwave end.

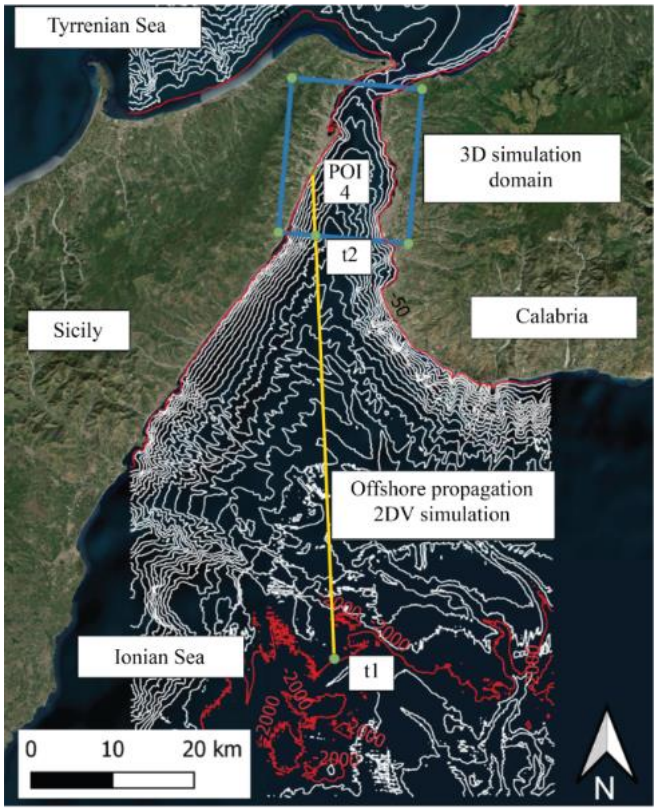

Figure 31: Numerical domains schematisation and detailed application of step II.

Subsequently, to apply step III, the numerical domain for the inundation simulations was defined as the blue area shown in Figure 31. The computational domain, covering approximately 14 km × 17 km, is presented in Figure 30 and features a variable spatial resolution ranging from 20 m to 10 m near the areas of interest. A weakly reflective condition was imposed at the offshore boundary, while the water surface elevation time series extracted at point t2 from step II were used as input. Wave reflection along the northern boundary was prevented through the implementation of a sponge layer combined with a radiation boundary condition. Furthermore, to ensure the applicability of the procedure to a broader range of tsunami inundation models, many of which do not support spatially varying bottom friction coefficients (e.g., Tsunami-HYSEA, as applied by (Tonini et al., 2021), a uniform Manning coefficient of 0.019 was adopted. Given the limited tidal range (approximately 20 cm) across the study area, and more generally throughout the Mediterranean Sea, no tidal phase synchronization was required. Each inundation simulation required approximately 5 to 10 days of computational time using 10 CPU cores on an Intel i7-10700K processor with 32 GB of RAM, depending on the selected tsunami wave period T.

3.2.c.3 Application of step I

Following step I of "DV6.3.2 Methodology Report", a circular area with a 40 km radius was delineated, centered on the geometric centroid of the triangle formed by connecting the three target locations shown in green in Figure 32a. This approach enabled the identification of seven distinct Points of Interest (POIs), which were subsequently used to define the MIHd. The hazard probability curves at the 84th percentile for each POI are presented in Figure 32b, indicating that POI 4 consistently exhibits the highest MIH value.

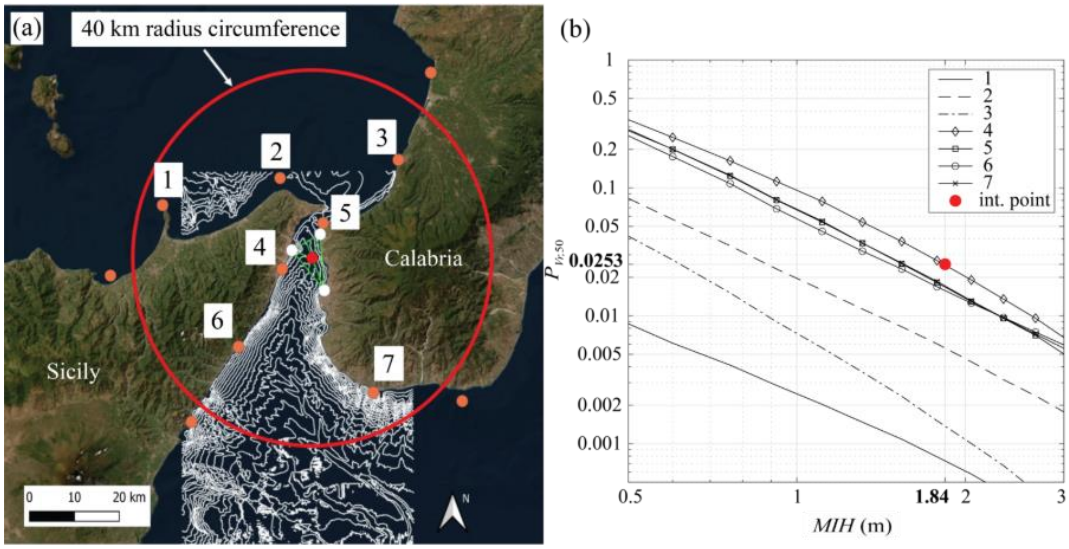

Figure 32: Definition of the Points of Interest (POIs) and computation of MIHd: (a) map showing the selected POIs, and (b) hazard probability curves at the 84th percentile for each POI. The red circle highlights the intersection between Pevr and the hazard curve of POI 4.

After selecting the POI, the values of the exceedance probability P_{vr} and the exposure time V_n were defined. In this example, the Italian Design Guidelines (Norme Tecniche per Lecostruzioni - Aggiornamento Delle "Norme Tecniche per Le Costruzioni", 2018), commonly adopted for seismic structural design, were followed. Accordingly, by applying the Structural Collapse Limit (SLC) approach, P_{vr} was set to 5% and V_n to 100 years for the infrastructures considered. Using:

$$ARP = -\frac{Vn}{ln(1 - Pvr)} \quad (3.2.2)$$

an Average Return Period (ARP) of 1,950 years was obtained. Subsequently:

$$P_{vr(MIH \geq MIH_d)} = 1 - \left(1 - \frac{1}{ARP}\right)^{V_n} \quad (3.2.3)$$

was applied to derive an equivalent probability of exceedance $P_{e,vr} = 0.0253$ for $V_n = 50$ years, which was then used to determine MIHd = 1.84 m from the hazard curves shown in Figure 32b. It is important to note that, under the assumptions of this study, MIHd corresponds to the wave amplitude at a water depth h = −50 m.

3.2.c.4 Application of step II

Three representative leading depression (LD) N-waves with different periods (T = 240 s, 1000 s, and 2000 s) within the range 120–3600 s (Basili & Brizuela, 2018) were selected as examples and used throughout the application of the proposed methodology in the Messina Strait. LD N-waves were chosen because they generally produce higher run-up values than leading elevation (LE) N-waves (Tadepalli & Synolakis, 1994) and are more representative of tsunamis that have not undergone long-distance propagation, a realistic assumption for the Mediterranean context. Using the selected T values and following the workflow outlined in DV 6-3.2, the mild-slope condition was verified on the offshore bathymetry near POI 4. As shown in Figure 31, this condition was satisfied for depths greater than 2000 m south of the Messina Strait, where point t1 was defined as the offshore propagation boundary. This location was selected due to its unobstructed path toward POI 4 and proximity to active faults identified in the Italian Database of Seismological Sources (DISS, 2021), which may represent potential tsunamigenic sources.

Only one offshore direction was considered, primarily for demonstrative purposes. This direction minimizes diffraction effects from the Calabrian coast and allows the simulation of wave propagation through the entire Strait, including potential re-reflections between the coastlines that can influence inundation. For each period T, a set of input surface elevation time series with varying offshore amplitudes was propagated from t1 (h= 2000 m) to POI 4 (h = 50 m) until the condition MIHd= ai+ was met at POI 4.

Given the convergent geometry of the Messina Strait, the calibrated tsunami signals were then propagated using a quasi-2DV simulation up to point t2 (h = 780 m) to prevent reflections from shallower areas. These results were subsequently used as boundary inputs for the larger, high-resolution inundation domain (shown in blue in Figure 31). Results for the case with T = 240 s are presented in Figure 33, where panel (b) shows the adjusted time t′, with t′ = 0 s corresponding to the arrival of each N-wave at t2. This adjustment was applied to reduce computational time.

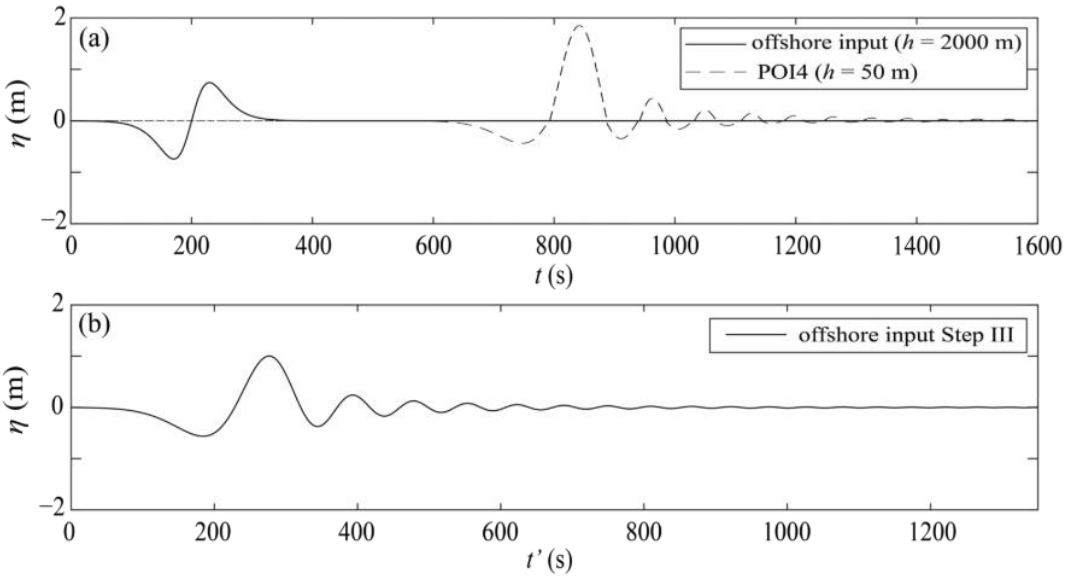

Figure 33: Example time series of the N-wave with T = 240 s: (a) offshore signal at t1 and propagated wave at POI 4; (b) input boundary condition for inundation at t2.

3.2.c.5 Application of step III

All inundation simulations were performed using the water surface elevation time series such the one defined in Section 3.2.c.4 as boundary conditions within the numerical setup described in Section 3.2.c.2. The areas associated to the largest hazard were the one of Villa San Giovanni and Messina. It is worth noting that, in Reggio Calabria, no flooding occurred near the railway station due to the presence of a retaining wall that effectively prevented inland water inundation. Villa San Giovanni presented the highest inundation hazard in the simulation with a wave period of T = 240 s. An oscillatory inundation pattern was observed inland, with a maximum flow depth of 3.5 m and a maximum flow velocity of 6.47 m/s. These results indicate that the central area of the Villa San Giovanni harbour is the most affected by tsunami hazard.

The inundation simulation results can be used to generate aggregated hazard maps to quantify the level of hazard in the inundated areas. Such maps are commonly employed during hazard assessment of infrastructure design projects. In the current study, the results for each area of interest and simulation were aggregated to produce hazard maps showing the maximum flow depth (hi) and the maximum depth-averaged velocity (V) across all simulations, corresponding to the three wave periods described in Section 3.2.c.4 and the respective time steps. In Figure 34, the extent of the aggregated maps for the simulations carried out in the current study is shown for the three interest areas. Here, the simplified inundation maps described in "DV6-3.2 Methodology Report" were also added using a red solid line. This comparison shows how the ISPRA maps are too conservative for design purposes also considering that, compared to the present approach, they do not contain information about the areal variability of hi. Note that, in the present document only the maps of hi were presented. A more complete hazard analysis of the area is reported in (Ruffini et al., 2025).

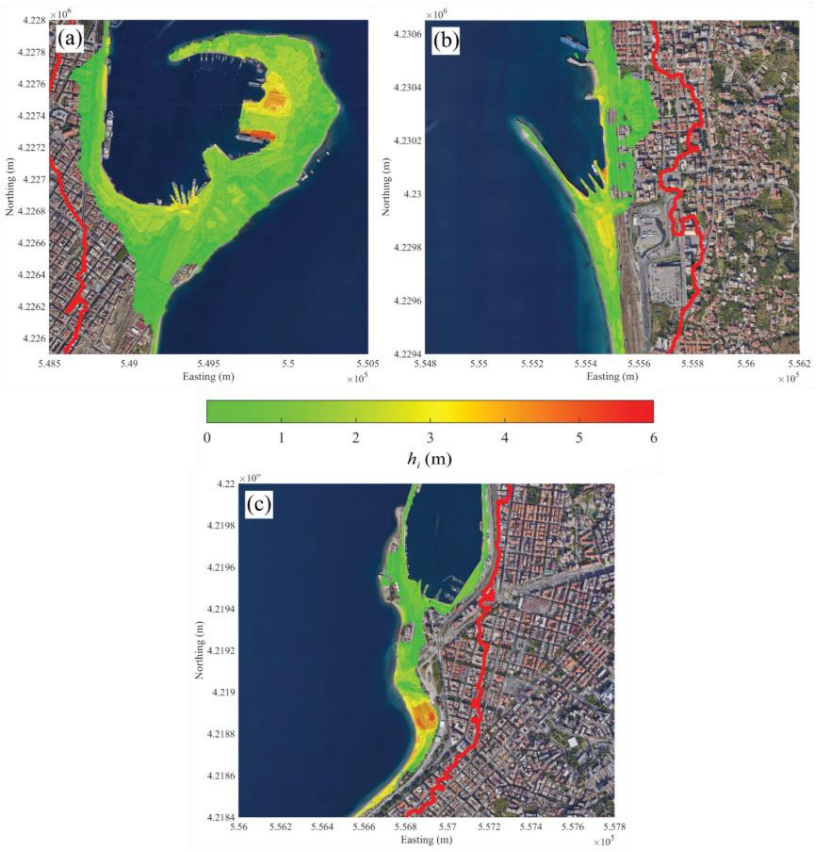

Figure 34: Aggregated hazard maps of the inundation depth hi for (a) Messina, (b) Villa San Giovanni, and (c) Reggio Calabria with inundation extents of simplified inundation maps from ISPRA.

5. References

Basili R, Brizuela B, Herrero A, et al. (2018). NEAMTHM18: online data of the probabilistic tsunami hazard model for the NEAM region from the TSUMAPS-NEAM project.

Carpanese, P., Badin, L., Follador, V., Ceresara, E.S., Donà, M., & da Porto, F. (2024). Identification and localization of critical industrial assets in Italy. In: Book of abstracts RETURN Dissemination Workshop, Torino, 1-2 February 2024. Eds: E. Costamagna, P. Mazzoglio.

Casson Moreno, V., Reniers, G., Salzano, E., & Cozzani, V. (2018). Analysis of physical and cyber security-related events in the chemical and process industry. *Process Safety and Environmental Protection*, 116, 621–631. https://doi.org/10.1016/j.psep.2018.03.026.

Castro Rodriguez, D. J., Beltramino, S., Scalas, M., Pilone, E., & Demichela, M. (2022). Territorial representation of a vulnerability associated with the Seveso installations in a Nord Italian case study. *Proceedings of the 32nd European Safety and Reliability Conference, ESREL 2022 - Understanding and Managing Risk and Reliability for a Sustainable Future*, 1463–1470. https://doi.org/10.3850/978-981-18-5183-4_R25-02-574-cd.

Castro Rodriguez, D. J. (2024). *Modelling Industrial Vulnerabilities within a Multi-hazard Framework for the Resilience of the Territories*. PhD Thesis. Politecnico di Torino, Turin, Italy.

Castro Rodriguez, D.J., Mietkiewicz, J., Vitale, M., Baldissone, G., Barresi, A.A., Demichela, M. (2024). NaTech triggered by lightning: Novel insights from past events in the process industry. *Heliyon*, 10. https://doi.org/10.1016/j.heliyon.2024.e31610.

Cimorelli, L., Covelli, C., De Vincenzo, A., Pianese, D., & Molino, B. (2021). Sedimentation in Reservoirs: Evaluation of Return Periods Related to Operational Failures of Water Supply Reservoirs with Monte Carlo Simulation. *Journal of Water Resources Planning and Management*, *147*(1), 1–12. https://doi.org/10.1061/(asce)wr.1943-5452.0001307.

Comitato Elettrico Italiano (2022). L*'applicazione online del CEI che consente l'accesso ai dati di DENSITÀ CERAUNICA*.

Dipartimento della Protezione Civile (2023). Classificazione Sismica al 31 di marzo di 2023. Ufficio II - Attività Tecnico Scientifiche per la prevenzione dei Rischi - Servizio Rischio Sismico.

DISS (2021). *Database of Individual Seismogenic Sources (DISS), Version 3.3.0: A compilation of potential sources for earthquakes larger than M 5.5 in Italy and surrounding areas*. https://diss.ingv.it/mapper/.

EMODnet Bathymetry Consortium (2022). *Emodnet digital bathymetry (DTM 2022)*. https://doi.org/https://doi.org/10.80212770/ff3aff8a-cff1-44a3-a2c8-1910bf109f85.

Ferlaino, F., Crescimanno, A., Dondona, C.A., Lella, L., & Rota, F. S. (2015). *Documento di inquadramento socioeconomico e territoriale per il piano strategico della Città Metropolitana di Torino*. Gruppo di ricerca IRES-Piemonte, Torino, Italia.

Gatti, F., Bonaventura, L., Menafoglio, A., Papini, M., & Longoni, L. (2023). A fully coupled superficial runoff and soil erosion basin scale model with efficient time stepping. *Computers and Geosciences*, *177*(March), 105362. https://doi.org/10.1016/j.cageo.2023.105362.

ISPRA (2023). *Inventario degli stabilimenti a rischio di incidenti rilevanti connessi con sostanze pericolose, Inventario Seveso D.Lgs. 105/2015*. https://www.rischioindustriale.isprambiente.gov.it/seveso-query-105/Default.php.

Kappes, M. S., Keiler, M., von Elverfeldt, K., & Glade, T. (2012). Challenges of analyzing multi-hazard risk: A review. *Natural Hazards*, *64*(2), 1925–1958. https://doi.org/10.1007/s11069-012-0294-2.

Krausmann, E., Renni, E., Campedel, M., & Cozzani, V. (2011). Industrial accidents triggered by earthquakes, floods and lightning: Lessons learned from a database analysis. *Natural Hazards*, *59*(1), 285–300. https://doi.org/10.1007/s11069-011-9754-3.

Krausmann, E., Köppke, K.-E., Fendler, R., Cruz, A.M., & Girgin, S. (2017). Chapter 8 - Qualitative and Semiquantitative Methods for Natech Risk Assessment. In: Krausmann, Elisabeth, Cruz, Ana Maria, Salzano, E. (Eds.), *Natech Risk Assessment and Management: Reducing the Risk of Natural-Hazard Impact on Hazardous Installations*. Elsevier, pp. 119–142. https://doi.org/10.1016/B978-0-12-803807-9.00008-5.

Manfreda, S., & Fiorentino, M. (2008). A stochastic approach for the description of the water balance dynamics in a river basin. *Hydrology and Earth System Sciences*, *12*(5), 1189–1200. https://doi.org/10.5194/hess-12-1189-2008.

Manfreda, S., Miglino, D., & Albertini, C. (2021). Impact of detention dams on the probability distribution of floods. *Hydrology and Earth System Sciences*, *25*(7), 4231–4242. https://doi.org/10.5194/hess-25-4231-2021.

Molino, B., Viparelli, R., & de Vincenzo, A. (2007). Effects of river network works and soil conservation measures on reservoir siltation. *International Journal of Sediment Research*, *22*(4), 273–281.

Molino, B., De Vincenzo, A., Minó, A., & Ambrosone, L. (2023). Long-Term Water Management Model for Preserving Sustainable Useful Capacity of Reservoirs. *Water Resources Management*, *37*(5), 1879–1894. https://doi.org/10.1007/s11269-023-03460-w.

Norme Tecniche per Lecostruzioni - Aggiornamento Delle "Norme Tecniche per Le Costruzioni" (2018). www.gazzettaufficiale.it/eli/id/2018/2/20/18A00716/.

Reniers, G., Khakzad, N., Cozzani, V., & Khan, F. (2018). The impact of nature on chemical industrial facilities: Dealing with challenges for creating resilient chemical industrial parks. *Journal of Loss Prevention in the Process Industries*, *56*, 378–385. https://doi.org/10.1016/j.jlp.2018.09.010.

Ricchiuti, A., Lotti, A., Astorri, F., Graziani, L., Maschio, G., Presti, G.L., Santucci, A., Ceci, P., Floridi, E., Favaroni, M. (2007). *Mappatura del rischio industriale in Italia*. (No. APAT, Rapporti XX/2007). Agenzia Nazionale per la Protezione dell'Ambiente e dei Servizi Tecnici (APAT).

Ricci, F., Casson Moreno, V., & Cozzani, V. (2021). A comprehensive analysis of the occurrence of Natech events in the process industry. *Process Safety and Environmental Protection*, *147*, 703–713. https://doi.org/10.1016/j.psep.2020.12.031.

Ruffini, G., Codato, C., Briganti, R., & De Girolamo, P. (2026). A methodology for tsunami inundation numerical simulations relying on inputs from probabilistic databases. *Natural Hazards*, 122, 109 (2026). https://doi.org/10.1007/s11069-025-07892-y.

Sabatino, R., Cordisco, A. (2013). *Protezione contro I fulmini: Valutazione del rischio*. Dipartimento Installazioni di Produzione e Insediamenti Antropici. ed. Istituto Nazionale Assicurazione contro gli Infortuni sul Lavoro (INAIL), Milano, Italy.

Tadepalli, S., & Synolakis, C. E. (1994). The run-up of N-waves on sloping beaches. *Proceedings - Royal Society of London, A*, *445*(1923), 99–112. https://doi.org/10.1098/rspa.1994.0050.

Tilloy, A., Malamud, B. D., Winter, H., & Joly-Laugel, A. (2019). A review of quantification methodologies for multi-hazard interrelationships. *Earth-Science Reviews*, *196*. https://doi.org/10.1016/j.earscirev.2019.102881.

Tonini, R., Di Manna, P., Lorito, S., Selva, J., Volpe, M., Romano, F., Basili, R., Brizuela, B., Castro, M. J., de la Asunción, M., Di Bucci, D., Dolce, M., Garcia, A., Gibbons, S. J., Glimsdal, S., González-Vida, J. M., Løvholt, F., Macías, J., Piatanesi, A., … Vittori, E. (2021). Testing Tsunami Inundation Maps for Evacuation Planning in Italy. *Frontiers in Earth Science*, *9*. https://doi.org/10.3389/feart.2021.628061.

Viparelli, R. (2004). *Criteri di intervento attivo e passivo per contenere e ridurre l'interrimento degli invasi*.